

Communication-Efficient Federated Learning under Dynamic Device Arrival and Departure: Convergence Analysis and Algorithm Design

Zhan-Lun Chang, *Student Member, IEEE*, Dong-Jun Han, *Member, IEEE*, Seyyedali Hosseinalipour, *Senior Member, IEEE*, Mung Chiang, *Fellow, IEEE*, Christopher G. Brinton, *Senior Member, IEEE*

Abstract—Most federated learning (FL) approaches assume a fixed device set. However, real-world scenarios often involve devices dynamically joining or leaving the system, driven by, e.g., user mobility patterns or handovers across cell boundaries. This dynamic setting introduces unique challenges: (1) the optimization objective evolves with the active device set, unlike traditional FL’s static objective; and (2) the current global model may no longer serve as an effective initialization for subsequent rounds, potentially hindering adaptation, delaying convergence, and reducing resource efficiency. To address these challenges, we first provide a convergence analysis for FL under a dynamic device set, accounting for factors such as gradient noise, local training iterations, and data heterogeneity. Building on this analysis, we propose a model initialization algorithm that enables rapid adaptation whenever devices join or leave the network. Our key idea is to compute a weighted average of previous global models, guided by gradient similarity, to prioritize models trained on data distributions that closely align with the current device set, thereby accelerating recovery from distribution shifts in fewer training rounds. This plug-and-play algorithm is designed to integrate seamlessly with existing FL methods, offering broad applicability. Experiments demonstrate that our approach achieves convergence speedups typically an order of magnitude or more compared to baselines, which we show drastically reduces energy consumption to reach a target accuracy.

Index Terms—Artificial Intelligence, Distributed Machine Learning, Federated Learning.

I. INTRODUCTION

FEDERATED learning (FL) facilitates collaborative model training across a set of devices connected to a central server. In FL, each device performs local training using its local data, and uploads model updates to the server periodically for aggregation. The aggregated models are then broadcasted across the devices to initiate the next round. FL has found many applications in resource-constrained environments, including the Internet of Things (IoT) [1], [2], autonomous driving [3], and smart cities [4].

In conventional FL frameworks [5]–[8], the cohort of edge devices engaged in training is typically assumed to be static, implying the objective function is fixed. Nevertheless, in practice, the assumption of a static device set rarely holds in wireless edge networks, where user mobility and fluctuating coverage patterns drive continuous system dynamics. Devices

frequently traverse cell boundaries, triggering handovers that result in their departure from one federated system and potential entry into another. Similarly, time-varying channel conditions and finite battery capacities can force devices to drop out of the system entirely. Unlike static scenarios where a fixed device set simply “duty-cycles” due to intermittent connectivity, these mobility-driven events fundamentally alter the active topology of the network: as devices physically enter or exit the server’s coverage area, the system faces a structural evolution of the device set, necessitating a learning framework that can handle/track the available population in the network.

Illustrative Example: Figure 1 illustrates our problem setting as a generalization of traditional FL to support dynamic device populations. Standard FL approaches typically handle temporary device unavailability by adjusting for partial participation, yet they assume the underlying set of users and the resulting optimization goal w^* remain fixed indefinitely. We generalize this by structuring model training into distinct *sessions* to accommodate population changes in the system (traditional FL corresponds to one single session). As shown in the bottom panel of Figure 1, we aim to retain the ability to handle partial device participation within a session while simultaneously adapting to device turnover between sessions. In doing so, *the optimization goal will evolve from a single static target to a sequence of objectives specific to each session*. By carefully accounting for device arrivals and departures, our framework establishes a sequence of session-specific optimization targets; however, efficiently tracking these shifting goals is crucial to preventing model stagnation as well as minimizing time to (re-)convergence and the associated communication overhead. This leads to our key research question:

Question: *How can we design a plug-and-play method that (i) integrates with existing FL algorithms (e.g., FedProx [9], SCAFFOLD [10]) originally developed for static device sets within a single session and (ii) provides fast adaptation to the changing optimization goal $w^{(s)*}$ as the system transitions between sessions s ?*

Realizing this adaptation is non-trivial as the system operates blindly with respect to future device dynamics: since the server has no prior knowledge of which devices will join or leave the system, it cannot pre-calculate the optimal starting point for the next session. Furthermore, simply carrying over the global model from the previous session is often suboptimal as significant shifts in the underlying data distribution can render the old model stale, forcing the algorithm to waste communication rounds merely “removing” outdated information. In resource-constrained wireless networks, this slow re-convergence is unacceptable, as it directly translates to exces-

Z.-L. Chang, M. Chiang, and C. G. Brinton are with the Elmore Family School of Electrical and Computer Engineering, Purdue University, West Lafayette, IN 47907, USA.

D.-J. Han is with the Department of Computer Science and Engineering, Yonsei University, Seoul 03722, Republic of Korea.

S. Hosseinalipour is with the Department of Electrical Engineering, University at Buffalo–SUNY, Buffalo, NY 14260, USA.

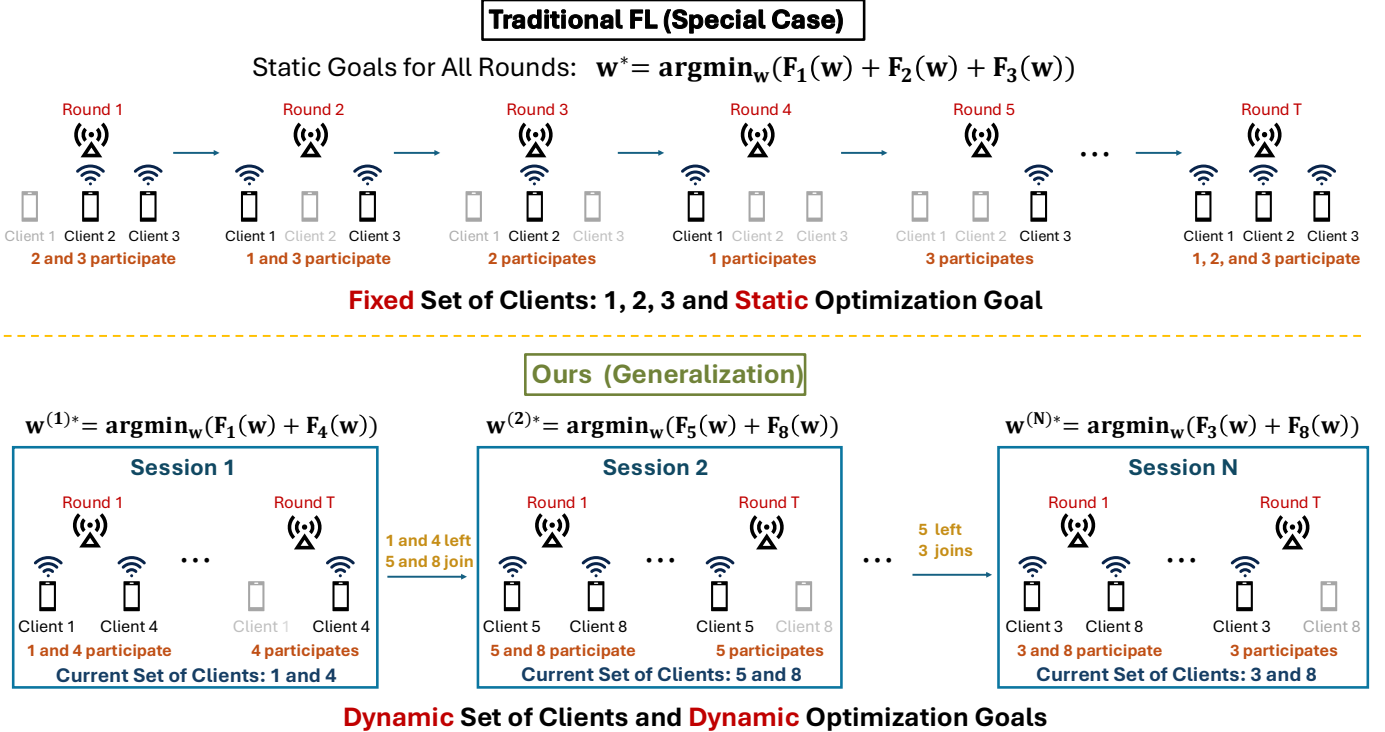


Fig. 1. Comparison illustrating our proposed dynamic FL framework as a generalization of traditional FL. Traditional FL represents the single-session special case, limited to a fixed device set and a static optimization goal. Our framework generalizes this structure to accommodate dynamic device arrivals and departures across multiple sessions, allowing the optimization goal to evolve and minimize the loss for the currently active set of users.

sive latency and higher energy consumption from executing more training rounds. The goal, therefore, is enabling fast global model re-convergence to reduce the resource overhead of each session.

Difference from Continual Learning: Unlike existing continual learning paradigms that aim to prevent catastrophic forgetting [11], which we consider in Section VI as one of our baselines, our work focuses on enabling *fast adaptation* to the current data distribution. This resembles a service provider aiming to build a global model that effectively serves the users who are currently active, motivated by wireless edge scenarios where devices frequently join and leave a local network. From this perspective, once a device leaves, the priority shifts to optimizing performance for the remaining users rather than preserving accuracy for those who have departed. We thus adopt a dynamic, session-centric view, emphasizing responsiveness to the active device population.

Summary of Contributions

To address the challenges introduced by dynamic device arrival and departure, this work makes the following key contributions:

- We conduct a novel theoretical analysis that analyzes the session-specific gradient norm under any pattern of device arrival and departure in dynamic FL. Our analysis considers a dynamic optimization objective, where each session aims to learn an optimized model that minimizes the loss function for the current devices. The bound incorporates critical factors influencing performance, including: (i) stochastic gradient noise arising from inherent randomness in local updates, (ii) the number of local training iterations, and (iii) the non-IID-ness of local data distributions.

- Building on our analysis, we propose a plug-and-play algorithm for dynamic optimization in FL, which constructs an effective initial model for each session. Aiming for low-complexity integration with existing FL methods (e.g., MOON [12], FedProx [9], SCAFFOLD [10], FedACG [13]), our algorithm initializes the model as a gradient similarity-weighted average of previous models, prioritizing models trained on devices whose data characteristics closely align with those of the current session. This approach accelerates model adaptation and mitigates costly performance drops caused by dynamic device participation.
- We evaluate system performance using two distinct metrics: *Time-to-Accuracy* and *Accumulated Accuracy Gain*. *Time-to-Accuracy* measures the number of global rounds required to recover a specific target accuracy, which translates to adaptation latency and energy consumption as well. Our results show that our strategy reduces the rounds needed to reach a target accuracy typically by an order of magnitude or more compared to continual learning baselines. Through communication and computation modeling, we quantify the corresponding improvements in energy consumption as well. Complementing this, the *Accumulated Accuracy Gain* metric confirms superior sustained performance throughout the session, yielding total accumulated accuracy gains of up to 8x in challenging zero-overlap session scenarios.

II. RELATED WORKS

FL has emerged as a prominent paradigm for distributed learning, enabling the collaborative training of models across devices while preserving data privacy [9], [14], [15]. One of the foundational works introduced the Federated Averaging (FedAvg) algorithm, which remains a cornerstone of many FL systems [14]. Subsequent studies have explored various

aspects of FL, including enhancing resource efficiency [4], [16]–[19], building robustness to adversarial attacks [20], [21], modeling energy consumption [22], and more distributed (non-star) topologies [4], [23]–[29]. However, these approaches typically assume a fixed set of participating devices throughout the training process, where devices are expected to remain available for the entire training duration [9]. This assumption simplifies the modeling of convergence and performance but does not adequately capture real-world scenarios characterized by dynamic device participation patterns.

To address the limitations of static device sets in FL, research on dynamic device selection and flexible participation has gained momentum, particularly in response to the challenges posed by varying device availability [7], [8], [30], [31]. These studies explore strategies such as optimizing device selection based on resource constraints, modeling participation patterns probabilistically, and employing adaptive algorithms to address the effects of non-IID (independent and identically distributed) data. In essence, the goal of these studies is to enhance overall model performance by strategically managing device participation during training, balancing computational efficiency, communication costs, and data representativeness. However, these works often assume a fixed device set, neglecting the dynamic nature of device arrival and departure. While [32] propose a flexible FL framework that allows for inactive devices, incomplete model updates, or dynamic device participation, their analysis is limited to scenarios where the optimization goal changes only once, specifically when a single device joins during training. This restricts the applicability of their approach to more complex and realistic patterns of device availability. Also, their analysis relies on more restrictive assumptions such as strong convexity and universally bounded gradient. There is also a line of work in continual FL [33], where the goal is to build a model that preserves all previously learned knowledge by preventing catastrophic forgetting. In contrast, as previously mentioned, our work focuses on rapidly adapting the global model to the current data distribution of devices. Given this difference in objectives, our approach significantly outperforms continual FL in scenarios involving dynamic device arrivals and departures, as we will show in Section VI.

III. SYSTEM MODEL AND THEORETICAL ANALYSIS

A. System Model

We discretize the FL process into discrete sessions, indexed by $s \in \{1, \dots, S\}$. Each session consists of T global training rounds, indexed by $t \in \{1, \dots, T\}$. To model device dynamics, $\mathcal{K}^{(s)} = \{1, \dots, K^{(s)}\}$ denotes the population of devices available in session s . Each device is connected to a central server and maintains its own ML model. Specifically, at session s , each device $k \in \mathcal{K}^{(s)}$ holds a dataset $\mathcal{D}_k^{(s)}$ of size $D_k^{(s)} \triangleq |\mathcal{D}_k^{(s)}|$, where each sample $d \in \mathcal{D}_k^{(s)}$ consists of a feature-label pair. A loss function $f(\mathbf{w}, d)$ evaluates model parameters $\mathbf{w} \in \mathbb{R}^M$ over individual samples. The local loss at device k during session s is defined as follows:

$$F_k^{(s)}(\mathbf{w}) \triangleq \sum_{d \in \mathcal{D}_k^{(s)}} f(\mathbf{w}, d) / D_k^{(s)}, \quad (1)$$

and the global loss function aggregates local losses over the current population:

$$F^{(s)}(\mathbf{w}) \triangleq \frac{1}{D^{(s)}} \sum_{k \in \mathcal{K}^{(s)}} D_k^{(s)} F_k^{(s)}(\mathbf{w}), \quad (2)$$

where $D^{(s)} \triangleq |\mathcal{D}^{(s)}|$ denotes the total number of data samples across all available devices in session s .

In our scenario of interest, where devices may join or leave at any time, the FL training objective evolves per session. As a result, the optimal global models form a sequence $\{\mathbf{w}^{(s)*}\}_{s=1}^S$, with each $\mathbf{w}^{(s)*}$ corresponding to the current session's data:

$$\mathbf{w}^{(s)*} = \arg \min_{\mathbf{w} \in \mathbb{R}^M} F^{(s)}(\mathbf{w}, \mathcal{D}^{(s)}). \quad (3)$$

This formulation is different from the traditional FL objectives (i.e., $\mathbf{w}^* = \arg \min_{\mathbf{w} \in \mathbb{R}^M} F(\mathbf{w}, \mathcal{D})$), which seeks a single model \mathbf{w}^* optimized over a fixed dataset \mathcal{D} . In contrast, our formulation targets a time-varying objective, optimizing $\mathbf{w}^{(s)*}$ based on the current/evolving data $\mathcal{D}^{(s)}$.

In our setting, each training round t in session s proceeds as follows. The server selects a set of participating devices $\mathcal{A}^{(s,t)} \subseteq \mathcal{K}^{(s)}$ and broadcasts the global model $\mathbf{w}^{(s,t)} \in \mathbb{R}^M$ to them. Each participating device k then updates the model using its data $\mathcal{D}_k^{(s)}$ over $e_k^{(s,t)}$ steps of stochastic gradient descent (SGD). Specifically, across SGD iterations $h \in \{0, \dots, e_k^{(s,t)} - 1\}$, the model update rule is as follows:

$$\mathbf{w}_k^{(s,t),h+1} = \mathbf{w}_k^{(s,t),h} - \eta^{(s,t)} \nabla F_k^{(s)}(\mathbf{w}_k^{(s,t),h}, \mathcal{B}_k^{(s,t)}), \quad (4)$$

where $\eta^{(s,t)}$ is the learning rate and $\mathcal{B}_k^{(s,t)} \subset \mathcal{D}_k^{(s)}$ is a mini-batch. The local training starts from the global model $\mathbf{w}_k^{(s,t),0} = \mathbf{w}^{(s,t)}$ and results in a final local model $\mathbf{w}_k^{(s,t),F}$. Devices send their final models to the server, which aggregates them as follows:

$$\mathbf{w}^{(s,t+1)} = \sum_{k \in \mathcal{A}^{(s,t)}} \frac{D_k^{(s)}}{\sum_{j \in \mathcal{A}^{(s,t)}} D_j^{(s)}} \mathbf{w}_k^{(s,t),F}. \quad (5)$$

The updated global model $\mathbf{w}^{(s,t+1)}$ is then broadcast to devices for the next training round.

B. Theoretical Analysis

To gain insights into how the FL algorithm performs in the complex system we consider, we first analyze its performance, which inspires the design of our proposed algorithm. We leverage the following two standard assumptions [34] to derive the analysis (henceforth, $\|\cdot\|$ denotes the two-norm).

Assumption 1 (Smoothness of Loss Functions). *Local loss function $F_k^{(s)}$ is β -smooth for all $k \in \mathcal{K}^{(s)}$, $\forall \mathbf{w}, \mathbf{w}' \in \mathbb{R}^M$, and s :*

$$\|\nabla F_k^{(s)}(\mathbf{w}) - \nabla F_k^{(s)}(\mathbf{w}')\| \leq \beta \|\mathbf{w} - \mathbf{w}'\|, \quad (6)$$

which implies the β -smoothness of the global loss function $F^{(s)}$ for all $s \in \{1, \dots, S\}$.

Assumption 2 (Bounded Dissimilarity of Local Loss Functions). *There exist finite constants $\zeta_1 \geq 1$, $\zeta_2 \geq 0$, such that*

for any set of coefficients $\{a_k \geq 0\}_{k \in \mathcal{K}^{(s)}}$ with $\sum_{k \in \mathcal{K}^{(s)}} a_k = 1$, the following holds for all s and \mathbf{w} :

$$\sum_{k \in \mathcal{K}^{(s)}} a_k \|\nabla F_k^{(s)}(\mathbf{w})\|^2 \leq \zeta_1 \left\| \sum_{k \in \mathcal{K}^{(s)}} a_k \nabla F_k^{(s)}(\mathbf{w}) \right\|^2 + \zeta_2. \quad (7)$$

To capture the heterogeneity within the local datasets of devices participating in a specific round, we introduce the concept of *local data variability*:

Definition 1 (Local Data Variability). *The local data variability at each device k is measured via $\Theta_k^{(s,t)} \geq 0$, which $\forall \mathbf{w}, k$ and $\forall d, d' \in \mathcal{D}_k^{(s)}$ satisfies*

$$\|\nabla f(\mathbf{w}, d) - \nabla f(\mathbf{w}, d')\| \leq \Theta_k^{(s,t)} \|d - d'\|. \quad (8)$$

We further define $\Theta^{(s,t)} = \max_{k \in \mathcal{K}^{(s)}} \{\Theta_k^{(s,t)}\}$.

We next obtain the convergence analysis for the non-convex loss function in the dynamic system.

Theorem 1 (Upper Bound on the Gradient Norm). *Suppose each device performs local SGD updates and the server aggregates via weighted averaging. Define $e_{\max}^{(s,t)} = \max_{k \in \mathcal{K}^{(s)}} e_k^{(s,t)}$ and $e_{\min}^{(s,t)} = \min_{k \in \mathcal{K}^{(s)}} e_k^{(s,t)}$. Assuming the learning rate $\eta^{(s,t)}$ satisfies*

$$\eta^{(s,t)} < \min \left\{ \left(0.5 - \left((e_{\min}^{(s,t)})^{-1} - 1 \right)^2 \right) \beta^{-1}, \left[\sqrt{\Lambda^{(s,t)}} \cdot \left(2\beta \sqrt{(\zeta_1 + \Lambda^{(s,t)}) e_{\max}^{(s,t)} (e_{\max}^{(s,t)} - 1)} \right) \right]^{-1} \right\},$$

where $\Lambda^{(s,t)} < 1$ is a constant, then for any pattern of device arrivals and departures, the cumulative average of the gradient of the global loss over S sessions and T rounds satisfies (9).

Proof. We present a sketch proof here and provide the detailed proof in our online technical report [35]. The convergence analysis relies on the β -smoothness of the global loss function $F^{(s)}(\cdot)$ and the bounding of error terms introduced by stochastic sampling and local updates as follows:

Step 1. Smoothness and Error Decomposition: Let $\mathbf{w}^{(s,t)}$ be the global model at round t of session s . Using the smoothness assumption, the expected descent in one global round is bounded by:

$$\begin{aligned} \mathbb{E}[F^{(s)}(\mathbf{w}^{(s,t+1)})] &\leq F^{(s)}(\mathbf{w}^{(s,t)}) \\ &- \eta^{(s,t)} \mathbb{E} \langle \nabla F^{(s)}(\mathbf{w}^{(s,t)}), \Delta^{(s,t)} \rangle + \frac{\beta(\eta^{(s,t)})^2}{2} \mathbb{E} \|\Delta^{(s,t)}\|^2, \end{aligned} \quad (10)$$

where $\Delta^{(s,t)} = \sum_{k \in \mathcal{A}^{(s,t)}} \frac{D_k^{(s)}}{\sum_{j \in \mathcal{A}^{(s,t)}} D_j^{(s)}} \nabla \bar{F}_k^{(s)}$ is the aggregated update direction derived from the participating set $\mathcal{A}^{(s,t)}$. Using the algebraic identity $2\langle \mathbf{a}, \mathbf{b} \rangle = \|\mathbf{a}\|^2 + \|\mathbf{b}\|^2 - \|\mathbf{a} - \mathbf{b}\|^2$, we decompose the inner product to isolate the ‘‘true’’ gradient norm. This yields:

$$\begin{aligned} \mathbb{E}[F^{(s)}(\mathbf{w}^{(s,t+1)})] &\leq F^{(s)}(\mathbf{w}^{(s,t)}) - \frac{\eta^{(s,t)}}{2} \|\nabla F^{(s)}(\mathbf{w}^{(s,t)})\|^2 \\ &+ \underbrace{\frac{\beta(\eta^{(s,t)})^2}{2} \mathbb{E} \|\Delta^{(s,t)}\|^2}_{\text{(A) Gradient Variance}} + \underbrace{\frac{\eta^{(s,t)}}{2} \mathbb{E} \|\nabla F^{(s)}(\mathbf{w}^{(s,t)}) - \Delta^{(s,t)}\|^2}_{\text{(B) Model Drift}}. \end{aligned} \quad (11)$$

Equation (11) highlights the two forces opposing convergence: the variance of the stochastic gradients (Term A) and the drift between the local accumulated gradients and the true global gradient (Term B).

Step 2. Bounding Gradient Variance (Term A): Unlike standard SGD analysis, our sampling is performed without replacement. Utilizing the properties of the hypergeometric distribution (finite population correction), we bound the variance of the mini-batch gradients. Specifically, we show that Term A has an upper bound:

$$\beta(\eta^{(s,t)})^2 (\Theta^{(s,t)})^2 \sum_{k \in \mathcal{K}^{(s)}} \frac{(\bar{\sigma}_k^{(s,t)})^2}{D_k^{(s)}} \sum_{e=1}^{e_k^{(s,t)}} \frac{1 - \frac{B_k^{(s,t)}}{D_k^{(s)}}}{B_k^{(s,t)}}. \quad (12)$$

Crucially, the factor $(1 - B_k^{(s,t)}/D_k^{(s)})$ captures the variance reduction: as the local batch size $B_k^{(s,t)}$ approaches the local dataset size $D_k^{(s)}$, the variance contribution vanishes.

Step 3. Bounding Model Drift (Term B): Since devices perform $e_k^{(s,t)}$ local steps, the local model $\mathbf{w}_k^{(s,t),e}$ drifts from $\mathbf{w}^{(s,t)}$. We bound this drift by recursively summing the squared norms of differences across local steps. The accumulated drift is bounded by:

$$\text{Term (B)} \leq \eta^{(s,t)} \mathcal{E}_{\text{var}} + \eta^{(s,t)} \mathcal{E}_{\text{grad}} \|\nabla F^{(s)}(\mathbf{w}^{(s,t)})\|^2, \quad (13)$$

where \mathcal{E}_{var} represents drift caused by noise and $\mathcal{E}_{\text{grad}}$ represents drift caused by the gradient direction itself.

Step 4. Final Convergence Bound: Substituting the bounds for Terms (A) and (B) back into (11), we group the coefficients of $\|\nabla F^{(s)}(\mathbf{w}^{(s,t)})\|^2$. To guarantee convergence, we require the step size $\eta^{(s,t)}$ to be sufficiently small such that the net coefficient is negative:

$$\eta^{(s,t)} \leq \frac{\sqrt{\Lambda^{(s,t)}}}{2\beta \sqrt{(\zeta_1 + \Lambda^{(s,t)}) e_{\max}^{(s,t)} (e_{\max}^{(s,t)} - 1)}}, \quad (14)$$

$$\begin{aligned} \frac{1}{ST} \sum_{s=1}^S \sum_{t=1}^T \mathbb{E} \|\nabla F^{(s)}(\mathbf{w}^{(s,t)})\|^2 &\leq \underbrace{\frac{1}{ST} \sum_{s=1}^S \sum_{t=1}^T \frac{2\mathbb{E}[F^{(s)}(\mathbf{w}^{(s,t)}) - F^{(s)}(\mathbf{w}^{(s,t+1)})]}{\eta^{(s,t)} (1 - \Lambda^{(s,t)})}}_{\text{(a)}} + \underbrace{\frac{1}{ST} \sum_{s=1}^S \sum_{t=1}^T \frac{4\beta(\Theta^{(s,t)})^2 \eta^{(s,t)}}{1 - \Lambda^{(s,t)}} \sum_{k \in \mathcal{K}^{(s)}} \frac{(\bar{\sigma}_k^{(s,t)})^2 e_k^{(s,t)} D_k^{(s)} - B_k^{(s,t)}}{B_k^{(s,t)} (D_k^{(s)})^2}}_{\text{(b)}} \\ &+ \underbrace{\frac{1}{ST} \left(\sum_{s=1}^S \sum_{t=1}^T \left(\frac{4\beta^2 (\eta^{(s,t)})^2}{D^{(s)} (1 - \Lambda^{(s,t)})} \sum_{k \in \mathcal{K}^{(s)}} (e_k^{(s,t)} - 1) \left(1 - \frac{B_k^{(s,t)}}{D_k^{(s)}} \right) \frac{\Theta^{(s,t)} (\bar{\sigma}_k^{(s,t)})^2}{B_k^{(s,t)}} \right) \right)}_{\text{(c)}} + \underbrace{\frac{1}{ST} \sum_{s=1}^S \sum_{t=1}^T 8\beta^2 (\eta^{(s,t)})^2 (e_{\max}^{(s,t)}) (e_{\max}^{(s,t)} - 1) \frac{\zeta_2}{1 - \Lambda^{(s,t)}}}_{\text{(d)}}. \end{aligned} \quad (9)$$

where $\Lambda^{(s,t)} < 1$ is a control parameter. Under this condition, telescoping the sum over S sessions and T rounds and rearranging yields the bound on $\frac{1}{ST} \sum_{s=1}^S \sum_{t=1}^T \|\nabla F^{(s)}(\mathbf{w}^{(s,t)})\|^2$ in Theorem 1. \square

Examining (9), term (a) reflects the expected improvement in the loss function at each training stage. (b) and (c) capture the negative impacts stemming from mini-batch sampling noise (controlled by batch size $B_k^{(s,t)}$), local data heterogeneity across devices (measured by $\Theta_k^{(s,t)}$), and the number of local SGD steps ($e_k^{(s,t)}$). Term (d) accounts for the influence of the maximum number of local SGD steps ($e_{\max}^{(s,t)}$) and inter-device model dissimilarity (represented by ζ_2).

Implications: Term (a) in (9) decomposes neatly into two contributions: $\mathbb{E}[F^{(s)}(\mathbf{w}^{(s,t)}) - F^{(s)}(\mathbf{w}^{(s)*})]$ and $\mathbb{E}[F^{(s)}(\mathbf{w}^{(s)*}) - F^{(s)}(\mathbf{w}^{(s,t+1)})]$. The second term arises from the update following round t and is beyond our control at that stage. Our algorithmic leverage lies in the first term, specifically at the session boundary ($t = 1$). By constructing an initial model $\mathbf{w}_{\text{init}}^{(s,1)}$ aiming to satisfy

$$\begin{aligned} & \mathbb{E}[F^{(s)}(\mathbf{w}_{\text{init}}^{(s,1)}) - F^{(s)}(\mathbf{w}^{(s)*})] \\ & \leq \mathbb{E}[F^{(s)}(\mathbf{w}^{(s-1,T+1)}) - F^{(s)}(\mathbf{w}^{(s)*})], \end{aligned} \quad (15)$$

we directly tighten the upper bound in Theorem 1 and reduce the cumulative average gradient norm. We next develop our algorithm for constructing the initial model $\mathbf{w}_{\text{init}}^{(s,1)}$ effectively.

IV. DYNAMIC INITIAL MODEL CONSTRUCTION

Pilot Preparation (Lines 5–12): The algorithm begins with a pilot preparation stage spanning the first P sessions. During this phase ($s \leq P$), the system performs standard FL training to build a history of model states. In each round t , a participating set of devices $\mathcal{A}^{(s,t)}$ trains locally on the current global model $\mathbf{w}^{(s,t)}$, and their updates are aggregated to form $\mathbf{w}^{(s,t+1)}$. The global model obtained at the end of each pilot session, $\mathbf{w}^{(s,T+1)}$, is saved to the repository Q_1 (Line 10). Upon completion of the P -th session (Line 11), the pilot model is derived by averaging these saved models (Line 12):

$$\mathbf{w}_{\text{Pilot}} = \frac{\sum_{s=1}^P \mathbf{w}^{(s,T+1)}}{P}. \quad (16)$$

These P saved global models are subsequently discarded to free memory. The pilot model's primary function is not to be an optimal model but to serve as an efficient, consistent baseline. While its simple average could be influenced by early-stage data heterogeneity, its value lies in providing a reference point for computing gradients, which capture the unique data distribution of each subsequent session. As shown in Section VI and Table IV, simple averaging yields performance comparable to that of a pilot model constructed via the exponential weighted average method.

Gradient Computation (Lines 14–22): Following the pilot stage, each new session s ($s > P$) initiates with a gradient computation process to capture the current data distribution. We introduce an auxiliary model sequence $\{\mathbf{w}_{\text{grad}}^{(s,v)}\}_{v=1}^{V+1}$, initialized using the pilot model: $\mathbf{w}_{\text{grad}}^{(s,1)} = \mathbf{w}_{\text{Pilot}}$. The system executes V global rounds (Line 17) on a sampled subset $\mathcal{A}_{\text{grad}}$, resulting

Algorithm 1 Dynamic Initial Model Construction

Require: T : global rounds per session, P : pilot preparation sessions, S : total sessions, V : gradient computation global rounds.

```

1: Initialize: Random global model  $\mathbf{w}^{(1,1)}$ , lists  $Q_1$  and  $Q_2$ , similarity scaling factor  $R$ .
2: for each session  $s = 1$  to  $S$  do:
3:   for each global round within session,  $t = 1$  to  $T$  do
4:     Pilot Preparation
5:     if  $s \leq P$  then
6:       for each device  $k \in \mathcal{A}^{(s,t)}$  do
7:         Local training on  $\mathbf{w}^{(s,t)}$  for  $e_k^{(s,t)}$  steps.
8:         Send final local model to the server.
9:       The server aggregates local models:  $\mathbf{w}^{(s,t+1)}$ .
10:      if  $t == T$  then Save  $\mathbf{w}^{(s,T+1)}$  to  $Q_1$ .
11:      if  $s == P$  and  $t == T$  then
12:        Compute pilot model  $\mathbf{w}_{\text{Pilot}} = \sum_{s=1}^P \mathbf{w}^{(s,T+1)} / P$ 
        and delete first  $P$  saved global models
         $\{\mathbf{w}^{(s,T+1)}\}_{s=1}^P$ .
13:     Gradient Computation (When A Session Starts)
14:     if  $s > P$  and  $t == 1$  then
15:        $\mathbf{w}_{\text{grad}}^{(s,1)} \leftarrow \mathbf{w}_{\text{Pilot}}$ 
16:       The server samples subset  $\mathcal{A}_{\text{grad}} \subseteq \mathcal{K}^{(s)}$ .
17:       for  $v = 1$  to  $V$  do
18:         for each device  $k \in \mathcal{A}_{\text{grad}}$  do
19:           Local training on  $\mathbf{w}_{\text{grad}}^{(s,1)}$  for  $e_k^{(s,1)}$  steps.
20:           Send final local model to the server.
21:         The server aggregates local models:  $\mathbf{w}_{\text{grad}}^{(s,v+1)}$ .
22:       Save  $G_s = \mathbf{w}_{\text{grad}}^{(s,V+1)} - \mathbf{w}_{\text{Pilot}}$  to  $Q_2$ .
23:     Initial Model Construction (When A Session Starts)
24:     if  $s > P + 1$  and  $t == 1$  then
25:       Compute  $\mathbf{w}_{\text{init}}^{(s,1)}$  using (18)
26:     Main Training
27:     if  $s > P$  then
28:       The server samples participating set  $\mathcal{A}^{(s,t)} \subseteq \mathcal{K}^{(s)}$ .
29:       for each device  $k \in \mathcal{A}^{(s,t)}$  do
30:         Training with Constructed Model
31:         if  $s > P + 1$  and  $t == 1$  then
32:            $\mathbf{w}^{(s,1)} \leftarrow \mathbf{w}_{\text{init}}^{(s,1)}$ 
33:           Local training on  $\mathbf{w}^{(s,t)}$  for  $e_k^{(s,t)}$  steps.
34:           Send final local model to the server.
35:         The server aggregates local models:  $\mathbf{w}^{(s,t+1)}$ .
36:       if  $t == T$  then: Save  $\mathbf{w}^{(s,T+1)}$  to  $Q_1$ .

```

in a final auxiliary model $\mathbf{w}_{\text{grad}}^{(s,V+1)}$. The *computed gradient* G_s is defined as the difference (Line 22):

$$G_s \triangleq \mathbf{w}_{\text{grad}}^{(s,V+1)} - \mathbf{w}_{\text{grad}}^{(s,1)} = \mathbf{w}_{\text{grad}}^{(s,V+1)} - \mathbf{w}_{\text{Pilot}}. \quad (17)$$

This quantity is particularly useful for evaluating the similarity between different data distributions, and its value is independent of the device data amount. For each session following the pilot preparation stage, only one computed gradient is retained.

Initial Model Construction (Lines 24–25): If sufficient history exists (i.e., $s > P + 1$), the system constructs a tailored initial model $\mathbf{w}_{\text{init}}^{(s,1)}$ before training begins. This is achieved using the saved models from previous sessions and the computed gradients:

$$\mathbf{w}_{\text{init}}^{(s,1)} \triangleq \sum_{z=P+1}^{s-1} \mu_{s,z} \mathbf{w}^{(z,T+1)}, \quad (18)$$

where

$$\mu_{s,z} = \frac{e^{-R\|G_s - G_z\|_2}}{\sum_{z=P+1}^{s-1} e^{-R\|G_s - G_z\|_2}}. \quad (19)$$

Illustration of the proposed algorithm: Total number of sessions (S) = 4, pilot preparation sessions (P) = 1

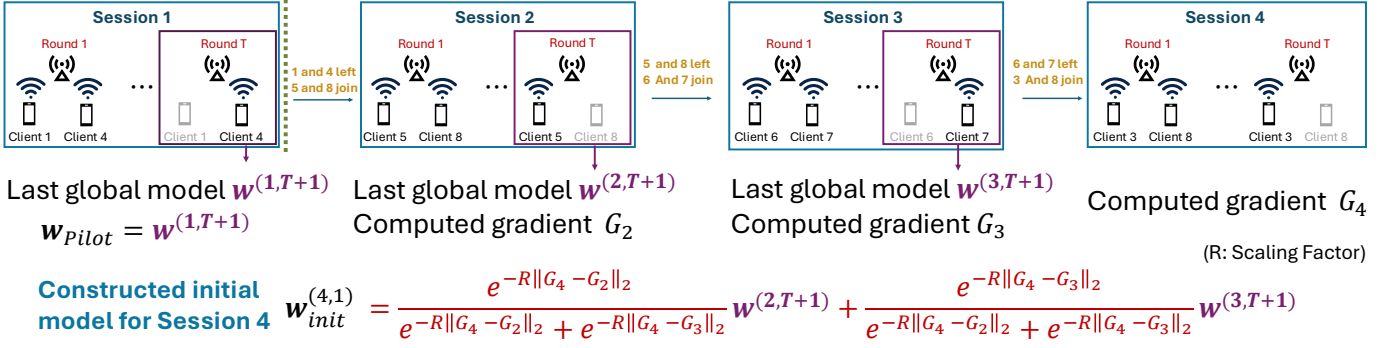


Fig. 2. Illustration of Algorithm 1 when the number of total sessions $S = 4$ and the number of pilot preparation sessions $P = 1$.

The update rule in (18) defines a weighted average of the saved models $w^{(z,T+1)}$. A small difference between the past computed gradient G_z and the current gradient G_s suggests that the data distribution in the z -th session is similar to that of the current session s . Consequently, a smaller $\|G_s - G_z\|_2$ yields a larger $\mu_{s,z}$, making the corresponding saved model a dominant component of the new initialization. The constant R in $\mu_{s,z}$ controls the sensitivity to gradient differences. When $R = 0$, the resulting initial model reduces to a simple average of all saved models from the pilot preparation stage, irrespective of data similarity. In contrast, as $R \rightarrow \infty$, the initial model converges to the single saved model corresponding to the most similar data distribution. As shown in Section VI and Table VI, our sensitivity analysis demonstrates that the performance of Algorithm 1 is robust across a wide range of R values.

Main Training (Line 27–36): The server samples participating devices $\mathcal{A}^{(s,t)}$ for the current round. A critical integration step occurs at the very start of the session (Lines 31–32): if a dynamic initial model $w_{init}^{(s,1)}$ was constructed ($s > P + 1$), the current global model is explicitly updated to this optimized starting point $w^{(s,1)} \leftarrow w_{init}^{(s,1)}$; otherwise, the session begins with the existing global model state. Devices then proceed with local training and model aggregation. Finally, the model obtained after the last round ($w^{(s,T+1)}$) is saved to the repository (Line 36) to facilitate future initializations.

Remark 1 (Practical Utility and Integration). *Our dynamic initial model construction algorithm provides an effective and easily integrated approach compatible with any FL method. Although providing formal guarantees for warm-start strategies is notoriously challenging [36], especially under device churn, theoretical insights (Theorem 1) and empirical validation in Section VI demonstrate its practical utility.*

V. COST ANALYSIS OF ALGORITHM 1

We analyze the communication, computation, and storage costs of Algorithm 1 on a stage-by-stage basis and discuss strategies to mitigate these costs in this section.

Pilot Model Construction

- **Computation:** Each of the P pilot sessions consists of T global rounds. In round t ($1 \leq t \leq T$) of session s , each participating device $k \in \mathcal{A}^{(s,t)}$ performs $e_k^{(s,t)}$ local epochs.

The total number of local epochs executed across all pilot sessions is therefore

$$\sum_{s=1}^P \sum_{t=1}^T \sum_{k \in \mathcal{A}^{(s,t)}} e_k^{(s,t)}.$$

- **Communication:** There are $P \times T$ global rounds in total. In each round t of session s , a set of $|\mathcal{A}^{(s,t)}|$ devices upload their locally trained models, and the server broadcasts the aggregated model. Consequently, the total number of transmissions consists of

$$\sum_{s=1}^P \sum_{t=1}^T |\mathcal{A}^{(s,t)}| \text{ (device uploads), } PT \text{ (server broadcasts),}$$

- **Storage:** Let Z denote the model size. The algorithm temporarily stores P intermediate models (the final model of each pilot session), each of size Z , and discards them after constructing the pilot model. The resulting temporary storage cost is therefore PZ .

Gradient Computation (for session s , $s \in \{P + 1, \dots, S\}$)

- **Computation:** Starting from the pilot model, the server performs V additional global rounds on a sampled subset $\mathcal{A}_{grad} \subseteq \mathcal{K}^{(s)}$. In each round $v \in \{1, \dots, V\}$, every device $k \in \mathcal{A}_{grad}$ runs $e_k^{(s,1)}$ local epochs, yielding a total computational load of

$$V \times \sum_{k \in \mathcal{A}_{grad}} e_k^{(s,1)}.$$

- **Communication:** Across these V rounds, each round incurs $|\mathcal{A}_{grad}|$ device uploads and one server broadcast. The total communication cost is therefore

$$V \times |\mathcal{A}_{grad}| \text{ (device uploads), } V \text{ (server broadcasts).}$$

- **Storage:** For each session s , a single gradient G_s of size Z is stored. Thus, as sessions progress, the storage for gradients grows linearly with the number of post-pilot sessions.

Coefficient Calculation (for session $s \in \{P + 1, \dots, S\}$)

- **Computation:** Computing softmax-based coefficients over the stored gradients from previous sessions incurs $O(s - (P + 1))$ cost for vector norms and exponentials.

Total Persistent Storage

- **Pilot model:** A single model w_{Pilot} of size Z is retained; all intermediate checkpoints are discarded.

- *Per post-pilot session s* : A final model checkpoint $w^{(s,T+1)}$ of size Z and a stored gradient G_s of size Z .
- *Overall growth*: The persistent storage grows linearly by $2Z$ per post-pilot session, resulting in a total increase proportional to $(S - P)$.

Justification for the Costs: The upfront cost of pilot training and gradient computation is offset by accelerated adaptation to shifting device distributions, reducing the total number of global rounds needed to achieve the target accuracy.

Mitigating Storage Cost: To bound storage growth, one may:

- *Limited history*: Retain only the most recent H sessions' models/gradients.
- *Selective retention*: Store models/gradients that maximize distributional diversity, preserving initialization quality with fewer saved models.

These strategies ensure manageable storage while maintaining algorithmic efficacy in dynamic federated learning settings.

VI. EXPERIMENTS

Seamless Integration with Representative FL Algorithms: To demonstrate the plug-and-play nature and broad applicability of our proposed initial model construction method, we integrate it with four representative and widely used FL algorithms: MOON [12], FedProx [9], SCAF-FOLD [10], and FedACG [13]. Notably, FedACG is the state-of-the-art method outperforming adaptive FL algorithms such as FedAvgM [37], FedADAM [38], and FedDyn [39]. Demonstrating compatibility with FedACG highlights that our approach can be effectively combined with the strongest modern FL algorithms. Importantly, our method does not replace these algorithms, but rather complements them by addressing the critical challenge of inter-session transition. These algorithms were originally developed for static device sets within a single session. Our method enhances their performance in dynamic multi-session settings by providing a well-initialized global model tailored for each session. In all experiments, the pilot model (w_{Pilot}) is fixed and reused across all sessions, taken from the last round of the first session. To construct the initialization for each subsequent session, we use only one global round ($V = 1$) to obtain the computed gradient.

Baselines: To the best of our knowledge, there is no existing work addressing the inter-session initialization problem in a dynamic FL system. Therefore, we construct three intuitive yet strong baselines to benchmark our method:

- **Previous:** Reuses the preceding session's model for continued training without explicitly constructing a new initial model [14].
- **Average:** Initializes models using the unweighted average of prior global models.
- **Continuous (image datasets only):** Uses Class-Semantic Relation Distillation Loss [33], anchoring the current model to the previous session's model to preserve class relationships while adapting to new data.

Task and Dataset: We perform classification tasks on seven diverse benchmarks, including six image datasets (MNIST [40], Fashion-MNIST [41], SVHN [42], CIFAR-10 [43], CIFAR-100 [43], TinyImageNet [43]) and the AG

TABLE I
SIMULATION PARAMETERS

Parameter	Value
<i>Network Geometry & Channel Model</i>	
Carrier Frequency (f_c)	3.5 GHz
Cell Radius (R_{cell})	250 m
Minimum Device Distance (d_{min})	10 m
BS Height (h_{BS})	10 m
User Terminal Height (h_{UT})	1.5 m
Environment Height (h_E)	1.0 m
Shadowing Standard Deviation (σ_{SF})	4 dB
Device Velocity (v_k)	10 m/s (36 km/h)
<i>Communication System</i>	
System Bandwidth (W)	100 MHz
Noise Power Spectral Density (N_0)	-174 dBm/Hz
Server Transmit Power ($P_{\text{server}}^{\text{tx}}$)	20 W (43 dBm)
Device Transmit Power (P_k^{tx})	200 mW (23 dBm)
Device Circuit Power (P_k^{cx})	100 mW
Time Slot Duration (τ)	0.5 ms
<i>Computation Model</i>	
CPU Clock Frequency (f_k)	1 GHz
Processor Efficiency (χ)	8 FLOPs/cycle
Effective Chipset Capacitance (ξ_k)	10^{-28}
<i>Model Specifications</i>	
MNIST Parameters ($N_p^{(\text{MNIST})}$)	7,850
MNIST Complexity ($\phi^{(\text{MNIST})}$)	2.00 FLOPs/Param
FMNIST Parameters ($N_p^{(\text{FMNIST})}$)	7,850
FMNIST Complexity ($\phi^{(\text{FMNIST})}$)	2.00 FLOPs/Param
SVHN Parameters ($N_p^{(\text{SVHN})}$)	667,178
SVHN Complexity ($\phi^{(\text{SVHN})}$)	91.04 FLOPs/Param
CIFAR-10 Parameters ($N_p^{(\text{C-10})}$)	11,573,066
CIFAR-10 Complexity ($\phi^{(\text{C-10})}$)	6.50 FLOPs/Param
CIFAR-100 Parameters ($N_p^{(\text{C-100})}$)	11,596,196
CIFAR-100 Complexity ($\phi^{(\text{C-100})}$)	6.50 FLOPs/Param
TinyImageNet Params ($N_p^{(\text{TinyImg})}$)	21,730,056
TinyImageNet Complexity ($\phi^{(\text{TinyImg})}$)	27.69 FLOPs/Param
AG News Parameters ($N_p^{(\text{AGNews})}$)	9,157,804
AG News Complexity ($\phi^{(\text{AGNews})}$)	2.63×10^{-4} FLOPs/Param

News text corpus [44]. We show results for TinyImageNet and AG News in the main text, and the remainder in our online technical report [35].

Label Distribution: In our main experiments, we utilize 100 devices. Data samples are distributed among devices by defining the set of labels available within a training session. To introduce variation in the label distribution across the training process, the set of labels available in one training session can partially overlap with the set of labels available in a subsequent session. This overlap level can range from zero (meaning the label sets for consecutive sessions are disjoint) up to a value approaching one (meaning most labels are shared, with only a small fraction unique to each set). For the labels available in a session, they are distributed among the active devices using a Dirichlet distribution parameterized by α [14]. A smaller value of α results in a more heterogeneous distribution of labels across devices, leading to higher non-IIDness between devices. Conversely, a larger value of α yields a more homogeneous distribution of labels across devices.

Communication and Computation Model: To evaluate the real-world performance of Algorithm 1, we model the latency and energy constraints imposed by the wireless environment. We consider a Time Division Duplex (TDD) system to separate uplink and downlink transmission intervals. Within each

interval, we assume an Orthogonal Frequency Division Multiple Access (OFDMA) scheme where devices are assigned orthogonal resource blocks (frequency channels), ensuring an interference-free environment.

1) *Channel Modeling*: The wireless channel between device k and the server is characterized by both large-scale and small-scale fading. The total channel gain $g_k[n]$ at time slot n is given by:

$$|g_k[n]|^2 = \psi_k \cdot |h_k[n]|^2, \quad (20)$$

where ψ_k denotes the *large-scale fading* coefficient and $h_k[n]$ represents the *small-scale fading* component.

For the large-scale fading models, we adopt the 3GPP Urban Micro (UMi) Street Canyon model defined in the technical report TR 38.901 [45], which is the standard for 5G/6G simulations in dense urban environments. The large-scale fading coefficient ψ_k captures the combined impact of path loss and shadowing. Shadowing is modeled via a random variable ξ following a zero-mean Gaussian distribution, denoted as $\xi \sim \mathcal{N}(0, \sigma_{SF}^2)$. For the UMi-LoS scenario, the standard deviation is defined as $\sigma_{SF} = 4$ dB. Accordingly, the total path loss, encompassing both propagation loss and shadowing, is expressed as $PL_{UMi-LoS} + \xi$ where $PL_{UMi-LoS}$ is the Line-of-Sight (LoS) path loss for Urban Micro scenario. Consequently, the linear large-scale fading coefficient ψ_k is obtained by converting the total path loss from the logarithmic scale:

$$\psi_k = 10^{-(PL_{UMi-LoS} + \xi)/10}. \quad (21)$$

We assume ψ_k remains constant during a single communication round.

We consider a single-cell system where the server (BS) is positioned at the center of a circular coverage area. The device locations are modeled as a Poisson Point Process (PPP) with uniform areal density within the cell, conditioned on a cell radius of $R_{\text{cell}} = 250$ m and a minimum distance of $d_{\text{min}} = 10$ m to ensure the validity of the path loss model. To satisfy the uniform areal density requirement, the Euclidean 2D distance $d_{2D,k}$ of device k from the BS follows the probability density function (PDF):

$$f(d) = \frac{2d}{R_{\text{cell}}^2 - d_{\text{min}}^2}, \quad d_{\text{min}} \leq d \leq R_{\text{cell}}. \quad (22)$$

The resulting 3D distance used in the path loss calculation is then given by $d_{3D,k} = \sqrt{d_{2D,k}^2 + (h_{\text{BS}} - h_{\text{UT}})^2}$.

The small-scale fading factor $h_k[n]$ is modeled as a first-order time-varying Gauss-Markov process:

$$h_k[n] = \rho_k h_k[n-1] + \sqrt{1 - \rho_k^2} e_k[n], \quad (23)$$

where $e_k[n] \sim \mathcal{CN}(0, 1)$ is an independent and identically distributed (i.i.d.) circularly symmetric complex Gaussian random variable. This term $e_k[n]$ introduces uncorrelated random fluctuations into the channel state. Consequently, the magnitude $|h_k[n]|$ follows a Rayleigh distribution [46], which effectively models a dense scattering wireless environment.

2) *Instantaneous Data Rate*: Based on the TDD assumption, the uplink and downlink channels share the same small-scale fading coefficient $h_k[n]$ within a time slot. The *Uplink Instantaneous Data Rate* (from device k to the server) at time slot n is calculated as:

$$R_k^{\text{UL}}[n] = W \log_2 \left(1 + \frac{P_k^{\text{tx}} \psi_k |h_k[n]|^2}{N_0 W} \right), \quad (24)$$

where W denotes the allocated channel bandwidth per device (Hz), P_k^{tx} is the transmission power of device k , and N_0 is the noise power spectral density.

Conversely, the *Downlink Instantaneous Data Rate* (from the server to device k) is given by:

$$R_k^{\text{DL}}[n] = W \log_2 \left(1 + \frac{P_{\text{server}}^{\text{tx}} \psi_k |h_k[n]|^2}{N_0 W} \right), \quad (25)$$

where $P_{\text{server}}^{\text{tx}}$ is the transmission power of the server. Note that typically $P_{\text{server}}^{\text{tx}} \gg P_k^{\text{tx}}$, resulting in higher downlink rates.

3) *Round-Trip Latency*: The total latency for a complete FL round involves the downlink transmission of the global model and the uplink transmission of the local model updates. Let Z denote the size of the model parameters in bits. Since the data rate varies over time, the transmission time is calculated by accumulating the instantaneous rate over discrete time slots of duration τ . The total round-trip communication latency T_k^{comm} for device k is: $T_k^{\text{comm}} = T_k^{\text{DL}} + T_k^{\text{UL}}$, where the downlink time T_k^{DL} and uplink time T_k^{UL} are the minimum durations required to satisfy:

$$\sum_{n=1}^{T_k^{\text{DL}}/\tau} R_k^{\text{DL}}[n] \cdot \tau \geq Z \quad \text{and} \quad \sum_{n=1}^{T_k^{\text{UL}}/\tau} R_k^{\text{UL}}[n] \cdot \tau \geq Z. \quad (26)$$

4) *Communication Energy Consumption*: We focus on the energy consumption of the devices, as they are typically battery-constrained. The total communication energy for device k , denoted as E_k^{comm} , comprises the energy required for receiving the global model (downlink) and transmitting the local update (uplink): $E_k^{\text{comm}} = E_k^{\text{DL}} + E_k^{\text{UL}}$. The downlink energy consumption is determined by the receiving circuit power P_k^{rx} and the downlink duration: $E_k^{\text{DL}} = P_k^{\text{rx}} \cdot T_k^{\text{DL}}$. The uplink energy consumption is determined by the transmission power P_k^{tx} and the uplink duration: $E_k^{\text{UL}} = P_k^{\text{tx}} \cdot T_k^{\text{UL}}$. Note that typically $P_k^{\text{tx}} \gg P_k^{\text{rx}}$, making the uplink transmission the dominant factor in communication energy consumption.

5) *Local Model Computation*: The local computation latency is determined by the complexity of the specific neural network architecture \mathcal{M} employed for the learning task and the device's processor efficiency. Let $N_p(\mathcal{M})$ denote the number of trainable parameters in model \mathcal{M} . We define $\phi(\mathcal{M})$ as the computational density ratio, representing the number of floating point operations (FLOPs) required per parameter for a full forward and backward propagation (FLOPs/param). Consequently, the computational workload to process a single data sample is given by $N_p(\mathcal{M}) \cdot \phi(\mathcal{M})$ FLOPs.

To account for hardware capabilities such as instruction-level parallelism (e.g., SIMD instructions), let χ denote the processor efficiency, defined as the number of FLOPs the CPU can execute per clock cycle (FLOPs/cycle). Given that device

TABLE II
PERFORMANCE COMPARISON OF IMPLEMENTING ALGORITHM 1 WITH MOON, FEDPROX, SCAFFOLD AND FEDACG UNDER DIFFERENT LABEL DISTRIBUTIONS FOR TINYIMAGENET DATASET FOR A SYSTEM WITH 100 DEVICES.

Dataset	Overlap	Dirichlet α	FL Alg.	Second Session Transition				Fourth Session Transition			
				Proposed	Continuous	Previous	Average	Proposed	Continuous	Previous	Average
TinyImageNet	0.0 (Non-Overlap)	0.3	MOON	65.98±0.30	56.16±0.26	58.58±0.51	58.15±0.33	67.03±0.42	57.64±0.67	61.71±0.79	62.57±0.45
			FedProx	65.33±0.30	56.03±0.31	63.03±0.36	61.15±0.38	66.56±0.41	57.57±0.48	64.73±0.14	63.80±0.22
			SCAFFOLD	67.51±0.17	52.43±0.92	60.19±0.26	61.66±0.24	68.47±0.23	54.64±0.65	61.11±0.38	63.81±0.27
			FedACG	66.54±0.19	56.05±0.34	32.99±3.50	55.69±1.47	67.11±0.47	57.78±0.50	36.26±1.55	62.29±0.35
	0.7	MOON	66.29±0.47	57.73±0.29	59.72±0.70	61.17±0.57	67.77±0.32	58.79±0.42	62.64±0.55	64.33±0.33	
		FedProx	66.21±0.21	57.71±0.35	63.88±0.22	61.98±0.37	67.26±0.16	58.75±0.46	65.25±0.39	64.40±0.21	
		SCAFFOLD	68.55±0.35	55.33±0.63	60.67±0.54	62.50±0.32	69.23±0.41	56.46±0.41	61.12±0.85	64.71±0.28	
		FedACG	66.71±0.43	57.74±0.29	38.89±2.21	58.76±1.20	67.84±0.28	58.78±0.41	31.27±2.123	63.96±0.30	
	0.2 (Slight Overlap)	0.3	MOON	64.99±0.66	58.67±0.35	60.88±0.51	60.79±0.29	66.36±0.61	59.79±0.42	61.91±0.54	62.98±0.27
			FedProx	65.48±0.43	58.64±0.26	63.75±0.17	60.47±0.35	66.32±0.32	59.80±0.43	65.38±0.28	63.45±0.50
			SCAFFOLD	67.58±0.46	56.77±0.49	60.84±0.45	62.22±0.38	68.09±0.31	57.66±0.69	61.35±0.57	64.48±0.45
			FedACG	66.33±0.70	58.65±0.35	57.24±0.51	58.62±0.42	66.39±0.40	59.84±0.48	55.29±0.96	62.42±0.49
0.7	MOON	66.09±0.58	59.94±0.41	62.47±0.20	62.56±0.28	67.03±0.39	60.69±0.52	63.18±0.49	64.20±0.22		
	FedProx	66.06±0.22	60.00±0.51	64.40±0.17	61.49±0.31	67.06±0.31	60.58±0.54	65.46±0.22	64.06±0.38		
	SCAFFOLD	68.30±0.19	58.53±0.50	61.07±0.41	63.57±0.25	68.83±0.33	58.76±0.41	61.16±0.28	65.35±0.40		
	FedACG	66.51±0.34	60.02±0.42	56.94±0.73	61.96±0.45	67.06±0.12	60.58±0.44	56.75±0.72	63.95±0.36		

TABLE III
PERFORMANCE COMPARISON OF IMPLEMENTING ALGORITHM 1 WITH MOON, FEDPROX, SCAFFOLD AND FEDACG UNDER DIFFERENT LABEL DISTRIBUTIONS FOR THE AG NEWS DATASET WITH 100 DEVICES.

Dataset	Overlap	Dirichlet α	FL Alg.	Second Session Transition			Fourth Session Transition		
				Proposed	Previous	Average	Proposed	Previous	Average
AG News	0.0 (Non-Overlap)	0.3	MOON	73.94±1.43	14.04±0.29	14.22±0.23	75.19±1.35	14.34±0.31	24.60±2.00
			FedProx	73.89±1.43	14.03±0.28	14.20±0.21	75.10±1.41	14.34±0.31	24.33±1.95
			SCAFFOLD	66.46±2.18	12.66±0.36	12.86±0.18	69.33±1.78	13.44±0.45	13.85±0.25
			FedACG	76.27±1.28	14.52±0.30	16.95±1.06	77.18±1.41	14.78±0.29	35.19±2.65
	0.7	MOON	73.95±1.40	14.04±0.30	14.23±0.23	74.83±1.50	14.34±0.32	24.59±1.99	
		FedProx	73.90±1.40	14.03±0.29	14.20±0.21	74.75±1.56	14.34±0.31	24.32±1.93	
		SCAFFOLD	66.64±2.14	12.63±0.21	12.88±0.18	68.99±3.04	13.24±0.16	13.89±0.26	
		FedACG	76.25±1.28	14.52±0.29	16.96±1.06	76.88±1.55	14.78±0.29	35.19±2.64	
	0.8 (Significant Overlap)	0.3	MOON	59.15±0.66	51.98±0.85	53.36±0.85	60.78±1.19	52.97±0.83	53.94±0.97
			FedProx	59.05±0.62	51.96±0.83	53.34±0.85	60.54±1.31	52.96±0.83	53.93±0.96
			SCAFFOLD	47.26±0.62	48.35±0.39	48.58±1.07	49.11±1.25	50.09±0.52	49.48±0.96
			FedACG	63.95±0.28	52.89±0.76	55.26±0.66	65.28±0.90	53.83±0.57	55.82±0.51
0.7	MOON	59.20±0.67	51.99±0.83	53.36±0.85	60.48±0.26	52.97±0.83	53.95±0.98		
	FedProx	59.09±0.65	51.97±0.83	53.34±0.84	60.27±0.34	52.96±0.83	53.92±0.98		
	SCAFFOLD	47.37±0.61	48.87±0.21	48.73±1.07	48.68±0.72	50.42±0.27	49.58±1.00		
	FedACG	63.95±0.29	52.92±0.75	55.26±0.66	64.54±0.36	53.84±0.59	55.83±0.50		

k performs $e_k^{(s,t)}$ local SGD iterations with a mini-batch size of $B^{(s,t)}$ during round t of session s , the local computation time T_k^{comp} is formulated as:

$$T_k^{\text{comp}} = \frac{N_p(\mathcal{M}) \cdot \phi(\mathcal{M}) \cdot e_k^{(s,t)} \cdot B^{(s,t)}}{f_k \cdot \chi}, \quad (27)$$

where f_k is the CPU clock frequency of device k (in Hz).

The energy consumption is modeled based on the effective chipset capacitance ξ_k [47]. Since the required number of CPU cycles is inversely proportional to the processor efficiency χ , the computation energy E_k^{comp} is given by:

$$E_k^{\text{comp}} = \xi_k \left(\frac{N_p(\mathcal{M}) \cdot \phi(\mathcal{M}) \cdot e_k^{(s,t)} \cdot B^{(s,t)}}{\chi} \right) (f_k)^2. \quad (28)$$

Parameter values used for simulating communication and computation are listed in Table I.

Performance Comparison and Analysis: Table II and Table III report the mean accuracy \pm standard deviation across three random seeds for our proposed initialization

strategy combined with MOON, FedProx, SCAFFOLD, and FedACG, compared to baselines on Tiny-ImageNet and AG News in the initial rounds following each session transition. Across diverse datasets and distribution scenarios, our method effectively mitigates accuracy degradation arising from device dynamics. Even in significant overlap settings where Previous and Average baselines are theoretically favored, our method retains a competitive advantage. Minor exceptions occur with SCAFFOLD due to its inherent variance reduction mechanism. Crucially, our scheme achieves the target accuracy with significantly fewer communication rounds. This effectively saves communication costs compared to baselines that require extensive retraining.

These gains are achieved efficiently using only a single shared pilot model and one global round for gradient computation per session. Figure 3 visualizes this efficiency. Baselines suffer severe and instantaneous accuracy degradation at session transitions and often plummet to near zero accuracy. In contrast, our method avoids such drops. By incurring the

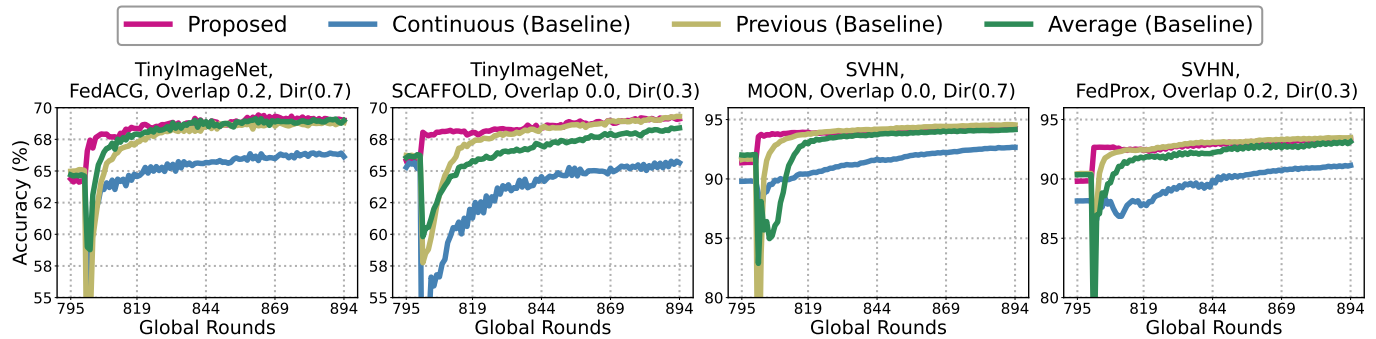


Fig. 3. Comparative performance analysis of the proposed algorithm against baseline FL methods across diverse datasets. The results validate that our scheme attains target accuracy with significantly fewer communication rounds, thereby effectively reducing communication costs under dynamic scenarios of device arrivals and departures.

TABLE IV
COMPARISON OF PILOT CONSTRUCTION METHODS FOR 9 TOTAL SESSIONS WITH 3 PILOT SESSIONS: AVERAGE VS. EXPONENTIALLY WEIGHTED AVERAGE (EMA) FOR SELECTED SCENARIOS. THE PERFORMANCE DIFFERENCE IS NEGLIGIBLE.

Dataset	Overlap	Dirichlet α	FL Alg.	Pilot Construction	Average Accuracy for Each Transition (%)			
					1st	2nd	3rd	4th
AG News	0.0	0.7	SCAFFOLD	Average	60.92±1.17	66.63±2.14	64.11±0.67	69.43±2.64
				EMA	60.92±1.17	66.63±2.14	64.15±0.71	69.62±2.39
SVHN	0.2	0.3	MOON	Average	89.69±0.78	93.28±0.17	91.26±0.38	93.81±0.12
				EMA	89.69±0.82	93.27±0.19	91.27±0.38	93.80±0.12
CIFAR-100	0.2	0.7	FedACG	Average	49.54±0.53	53.50±0.48	53.28±0.47	55.53±0.70
				EMA	49.82±0.28	53.69±0.43	53.02±0.52	55.90±0.46
TinyImageNet	0.0	0.3	FedProx	Average	62.02±0.38	65.88±0.28	63.93±0.22	67.18±0.23
				EMA	61.97±0.43	65.99±0.21	64.02±0.33	67.11±0.35

marginal cost of only one additional global round, our approach eliminates the need for the prolonged recovery phases observed in standard methods and offers a robust solution for dynamic FL systems.

Ablation Study (Different Pilot Construction Methods):

To validate the robustness of our pilot construction strategy, we investigate whether a more sophisticated aggregation method improves the quality of the generated initial models. Specifically, we compare our proposed simple average (Eq. 16) against an Exponentially Weighted Moving Average (EMA) construction. While the simple average assigns uniform importance ($1/P$) to all pilot sessions, the EMA approach prioritizes the most recent global models. Under the EMA scheme, the pilot model is computed as

$$\mathbf{w}_{\text{Pilot}}^{\text{EMA}} = \sum_{s=0}^{P-1} \gamma_s \mathbf{w}_s^{\text{last}}, \quad (29)$$

where the weighting coefficients γ_s are determined by a decay factor $\beta \in [0, 1)$ as follows:

$$\gamma_s = \begin{cases} \beta^{P-1}, & \text{if } s = 0 \text{ (oldest session),} \\ (1 - \beta)\beta^{P-1-s}, & \text{if } 0 < s \leq P - 1. \end{cases} \quad (30)$$

where $\sum_{s=0}^{P-1} \gamma_s = 1$. For example, with $P = 3$ pilot sessions, the aggregated pilot model is computed as: $\mathbf{w}_{\text{Pilot}}^{\text{EMA}} = \beta^2 \mathbf{w}_0^{\text{last}} + \beta(1 - \beta)\mathbf{w}_1^{\text{last}} + (1 - \beta)\mathbf{w}_2^{\text{last}}$. This pilot formulation theoretically adapts faster to recent trends in the data distribution.

Table IV presents the accuracy comparison across four distinct datasets and FL algorithms. We observe that the performance difference between the two methods is negligible across all scenarios. This consistency implies that the specific weighting of historical models in the pilot phase does not significantly alter the effectiveness of the subsequently computed gradients G_s . Consequently, we adopt the simple average in Algorithm 1, as it achieves competitive performance without introducing additional hyperparameters.

Ablation Study (Sensitivity Analysis of V): This study evaluates how the number of gradient computation rounds (V) affects the balance between performance stability and computational cost. While increasing V theoretically refines gradient estimation, the empirical results in Table V demonstrate that setting $V > 1$ yields negligible improvements. Accuracy fluctuations across all datasets remain within standard deviations; for instance, SVHN exhibits a difference of less than 0.03% between $V = 1$ and $V = 2$. Since computational and communication overheads scale linearly with V , we adopt $V = 1$ to maximize efficiency without compromising accuracy.

Sensitivity Analysis of Similarity Scaling Factor (R): We evaluate the algorithm's robustness to the scaling factor R , which regulates the sensitivity of the weighting coefficients $\mu_{s,z}$ to gradient differences. Table VI summarizes performance across R values tailored to the gradient norms of each dataset (e.g., higher magnitudes for AG News). The results indicate that the algorithm is highly stable across variations in R . Accuracy fluctuations are statistically negligible; for instance,

TABLE V
ABLATION STUDY ON THE NUMBER OF GRADIENT COMPUTATION ROUNDS (V). COMPARISON OF ACCURACY (MEAN \pm STD) FOR THE SECOND AND FOURTH SESSION TRANSITIONS. USING $V = 1$ PROVIDES THE BEST TRADE-OFF BETWEEN PERFORMANCE AND COMPUTATIONAL EFFICIENCY.

Dataset	Overlap	Dirichlet α	FL Alg.	2nd Session Transition Accuracy (%)			4th Session Transition Accuracy (%)		
				$V=1$	$V=2$	$V=3$	$V=1$	$V=2$	$V=3$
AG News	0.0	0.7	SCAFFOLD	66.64 \pm 2.14	66.62 \pm 2.18	66.63 \pm 2.16	68.99 \pm 3.04	69.80 \pm 2.39	69.51 \pm 2.41
SVHN	0.2	0.3	MOON	93.23 \pm 0.18	93.26 \pm 0.20	93.29 \pm 0.24	93.86 \pm 0.19	93.89 \pm 0.21	93.86 \pm 0.17
CIFAR-100	0.2	0.7	FedACG	53.52 \pm 0.14	52.91 \pm 0.60	53.00 \pm 0.79	55.82 \pm 0.26	55.42 \pm 0.24	55.17 \pm 0.58
TinyImageNet	0.0	0.3	FedProx	65.33 \pm 0.30	65.77 \pm 0.31	65.79 \pm 0.37	65.56 \pm 0.41	66.96 \pm 0.22	67.14 \pm 0.22

TABLE VI
SENSITIVITY ANALYSIS OF THE SIMILARITY SCALING FACTOR (R). COMPARISON OF ACCURACY (MEAN \pm STD) FOR THE SECOND AND FOURTH SESSION TRANSITIONS. THE ALGORITHM DEMONSTRATES ROBUSTNESS TO VARIATIONS IN R WITHIN REASONABLE RANGES.

Dataset (Values of R)	Overlap	Dirichlet α	FL Alg.	2nd Session Transition Accuracy (%)			4th Session Transition Accuracy (%)		
				Low R	Med R	High R	Low R	Med R	High R
AG News ($R \in \{800, 1000, 1200\}$)	0.0	0.7	SCAFFOLD	66.64 \pm 2.14	66.64 \pm 2.14	66.64 \pm 2.14	68.99 \pm 3.04	68.82 \pm 3.26	68.69 \pm 3.42
SVHN ($R \in \{10, 50, 100\}$)	0.2	0.3	MOON	93.23 \pm 0.18	93.26 \pm 0.19	93.25 \pm 0.19	93.86 \pm 0.19	93.88 \pm 0.21	93.89 \pm 0.23
CIFAR-100 ($R \in \{10, 50, 100\}$)	0.2	0.7	FedACG	53.52 \pm 0.14	53.61 \pm 0.48	53.62 \pm 0.41	55.82 \pm 0.26	55.91 \pm 1.03	55.57 \pm 1.25
Tiny ImageNet ($R \in \{10, 50, 100\}$)	0.0	0.3	FedProx	65.33 \pm 0.30	65.99 \pm 0.23	66.01 \pm 0.35	66.56 \pm 0.41	66.79 \pm 0.57	66.55 \pm 0.49

SVHN shows a variation of less than 0.1%, and the performance margins for AG News and CIFAR-100 largely overlap within standard deviations. This suggests that while R must be set to an appropriate order of magnitude, precise fine-tuning is not necessary to achieve good performance.

Quantification of Performance Gain: We quantify performance based on the model’s ability to rapidly adapt with two metrics: (1) *Time-to-Accuracy* and (2) *Accumulated Accuracy Gain*. *Time-to-Accuracy (Adaptation Speed)* metric measures the latency of adaptation following the start of a new session. It is defined as the number of global rounds t (within the current session s) required for an algorithm to recover to a specific percentage (ρ) of the peak accuracy achieved by the proposed scheme in that session. Let $Acc_s^{(alg)}(t)$ denote the accuracy of an algorithm at the t -th global round of session s , and let $Acc_{s,prop}^*$ be the maximum accuracy achieved by the proposed method within session s . The Time-to-Accuracy T_ρ is defined as:

$$T_\rho = \min\{t \in [1, T] \mid Acc_s^{(alg)}(t) \geq \rho \cdot Acc_{s,prop}^*\} \quad (31)$$

where T is the total number of global rounds per session, and $\rho \in \{0.95, 0.97\}$. A lower T_ρ indicates that the algorithm requires fewer global rounds (and consequently less latency and energy) to adapt to the new distribution. If the target is not reached within the session, T_ρ is denoted as ∞ .

While *Time-to-Accuracy* measures convergence speed to a specific target, it fails to capture the stability or sustained magnitude of performance throughout the session. To address this, we define the *Accumulated Accuracy Gain*, which quantifies the cumulative performance advantage of the proposed method over a baseline.

Calculated as the sum of accuracy differentials between the proposed method and a baseline b , the total gain G_{total} for session s is defined as:

$$G_{total} = \sum_{t=1}^T \left(Acc_s^{(prop)}(t) - Acc_s^{(b)}(t) \right) \quad (32)$$

A positive G_{total} indicates that the proposed method maintains a superior accuracy trajectory compared to the baseline across the session’s global rounds.

Table VII presents the quantitative results for Time-to-Accuracy and Accumulated Accuracy Gain, highlighting the efficiency of the proposed dynamic initialization strategy. The most significant advantage is the substantial reduction in latency and energy consumption, computed using our communication and computation model. Across all scenarios, the proposed method demonstrates rapid adaptation, consistently recovering the target accuracy in just a single round. In the challenging TinyImageNet tasks (specifically under the SCAFFOLD algorithm), this efficiency contrasts sharply with the *Continuous* baseline, which requires 150 rounds to reach the same threshold. This convergence gap translates into substantial resource savings; the proposed method consumes only 1.43 kJ of energy compared to the 214.33 kJ required by the Continuous baseline, representing a 150 \times reduction in resource overhead.

Furthermore, the *Accumulated Accuracy Gain* column confirms that the proposed method maintains a sustained performance advantage throughout the entire adaptation phase. This improvement is most pronounced in scenarios with zero overlap (e.g., SCAFFOLD on TinyImageNet), where our method yields a total accuracy gain of +867.1% over

TABLE VII
COMPARISON OF TIME-TO-ACCURACY (95% TARGET FOR TINYIMAGENET, 97% TARGET FOR SVHN) AND ACCUMULATED ACCURACY GAIN.

Dataset	Overlap	Dirichlet α	FL Alg.	Method	Time-to-Accuracy (95%/97% Target)				Accumulated
					Rounds	Latency (s)	Energy (kJ)	Speedup	Accuracy Gain (%)
TinyImageNet	0.2	0.7	FedACG	Proposed	1	113.6	1.43	—	—
				Previous (Baseline)	11	1,249.4	15.72	11.0×	+139.6
				Continuous (Baseline)	55	6,247.2	78.59	55.0×	+542.4
				Average (Baseline)	7	795.1	10.00	7.0×	+61.1
TinyImageNet	0.0	0.3	SCAFFOLD	Proposed	1	113.6	1.43	—	—
				Previous (Baseline)	14	1,590.2	20.00	14.0×	+85.7
				Continuous (Baseline)	150	17,037.7	214.33	150.0×	+867.1
				Average (Baseline)	28	3,180.4	40.01	28.0×	+243.5
SVHN	0.0	0.7	MOON	Proposed	1	6.9	0.08	—	—
				Previous (Baseline)	5	34.4	0.39	5.0×	+11.5
				Continuous (Baseline)	52	358.1	4.04	52.0×	+395.1
				Average (Baseline)	14	96.4	1.09	14.0×	+116.1
SVHN	0.2	0.3	FedProx	Proposed	1	6.9	0.08	—	—
				Previous (Baseline)	4	27.5	0.31	4.0×	+8.0
				Continuous (Baseline)	70	482.1	5.44	70.0×	+517.6
				Average (Baseline)	10	68.9	0.78	10.0×	+115.0

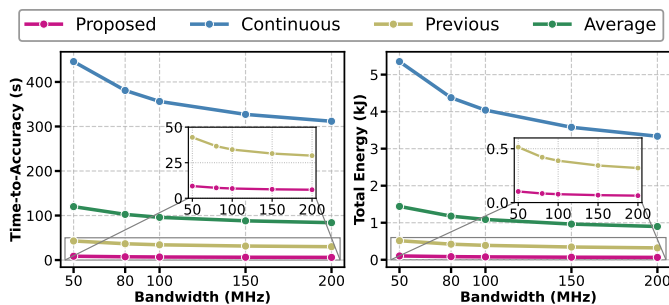


Fig. 4. Impact of system bandwidth on Total Latency (left) and Total Energy Consumption (right) required to reach 97% of the proposed scheme’s peak accuracy on the SVHN dataset. The proposed method consistently achieves the lowest latency and energy consumption across all bandwidth configurations (50–200 MHz). Insets highlight the performance gap between the Proposed and Previous schemes at a finer scale.

the Continuous baseline. Against the *Previous* baseline, our method consistently achieves positive total gains, validating that the proposed weighted initialization strategy provides a superior starting point compared to simply reusing the last session’s model.

Impact of System Bandwidth: We further investigate the robustness of the proposed framework to communication resource constraints by varying the system bandwidth from 50 MHz to 200 MHz. Figure 4 illustrates the total latency and energy consumption required to recover 97% of the maximum accuracy for our proposed scheme on the SVHN dataset. The results demonstrate that our method consistently achieves the target accuracy with fewer communication rounds. Consequently, our approach effectively saves communication costs and yields the lowest resource overhead across all bandwidth configurations. While higher bandwidth naturally reduces transmission time for all methods, the proposed algorithm maintains a distinct efficiency advantage as highlighted by the insets comparing it to *Previous* baseline. This confirms that the efficiency gains are driven by the reduction in required training rounds and algorithmic convergence rather than being dependent on specific channel conditions.

Other Experiments: Our online technical report [35] provides extensive supplementary results for our other benchmark

datasets (MNIST, Fashion-MNIST, SVHN, CIFAR-10, and CIFAR-100) across systems with varying devices. These additional experiments demonstrate the robustness of our approach under several alternative non-IID data distributions as well.

VII. CONCLUSION

In this paper, we addressed the structural challenges inherent to Federated Learning in wireless edge networks, specifically those driven by dynamic device arrival and departure. We presented a theoretical convergence analysis that explicitly accounts for the shifting optimization goals associated with evolving device sets, quantifying the impact of gradient noise and data heterogeneity. Guided by these theoretical insights, we proposed a plug-and-play initialization strategy that accelerates adaptation by constructing a weighted average of historical models based on gradient similarity. This approach effectively bridges distributional shifts between sessions without requiring server-side knowledge of future device activities. Extensive simulations demonstrate that our method achieves convergence speedups typically an order of magnitude or more compared to baselines and substantial energy savings compared to state-of-the-art baselines. Future work will focus on developing adaptive triggering mechanisms to determine when a new session initialization is required, further minimizing computational overhead in highly volatile environments.

REFERENCES

- [1] S. Wang, T. Tuor, T. Salonidis, K. K. Leung, C. Makaya, T. He, and K. Chan, “Adaptive federated learning in resource constrained edge computing systems,” *IEEE journal on selected areas in communications*, vol. 37, no. 6, pp. 1205–1221, 2019.
- [2] S. AbdulRahman, S. Otoum, O. Bouachir, and A. Mourad, “Management of digital twin-driven iot using federated learning,” *IEEE Journal on Selected Areas in Communications*, vol. 41, no. 11, pp. 3636–3649, 2023.
- [3] S. Samarakoon, M. Bennis, W. Saad, and M. Debbah, “Distributed federated learning for ultra-reliable low-latency vehicular communications,” *IEEE Transactions on Communications*, vol. 68, no. 2, pp. 1146–1159, 2019.
- [4] H. Xing, O. Simeone, and S. Bi, “Federated learning over wireless device-to-device networks: Algorithms and convergence analysis,” *IEEE Journal on Selected Areas in Communications*, vol. 39, no. 12, pp. 3723–3741, 2021.

- [5] C. T. Dinh, N. H. Tran, M. N. Nguyen, C. S. Hong, W. Bao, A. Y. Zomaya, and V. Gramoli, "Federated learning over wireless networks: Convergence analysis and resource allocation," *IEEE/ACM Transactions on Networking*, vol. 29, no. 1, pp. 398–409, 2020.
- [6] T. Xiang, Y. Bi, X. Chen, Y. Liu, B. Wang, X. Shen, and X. Wang, "Federated learning with dynamic epoch adjustment and collaborative training in mobile edge computing," *IEEE Transactions on Mobile Computing*, vol. 23, no. 5, pp. 4092–4106, 2023.
- [7] D. Jhunjhunwala, P. Sharma, A. Nagarkatti, and G. Joshi, "Fedvarp: Tackling the variance due to partial client participation in federated learning," in *Uncertainty in Artificial Intelligence*. PMLR, 2022, pp. 906–916.
- [8] J. Xu and H. Wang, "Client selection and bandwidth allocation in wireless federated learning networks: A long-term perspective," *IEEE Transactions on Wireless Communications*, vol. 20, no. 2, pp. 1188–1200, 2020.
- [9] T. Li, A. K. Sahu, M. Zaheer, M. Sanjabi, A. Talwalkar, and V. Smith, "Federated optimization in heterogeneous networks," *Proceedings of Machine Learning and Systems*, vol. 2, pp. 429–450, 2020.
- [10] S. P. Karimireddy, S. Kale, M. Mohri, S. J. Reddi, S. U. Stich, and A. T. Suresh, "Scaffold: Stochastic controlled averaging for on-device federated learning," in *Proceedings of the 37th International Conference on Machine Learning (ICML)*, 2020, pp. 5132–5143.
- [11] J. Yoon, W. Jeong, G. Lee, E. Yang, and S. J. Hwang, "Federated continual learning with weighted inter-client transfer," in *International Conference on Machine Learning*. PMLR, 2021, pp. 12073–12086.
- [12] Q. Li, B. He, and D. Song, "Model-contrastive federated learning," in *Proceedings of the IEEE/CVF conference on computer vision and pattern recognition*, 2021, pp. 10713–10722.
- [13] G. Kim, J. Kim, and B. Han, "Communication-efficient federated learning with accelerated client gradient," in *Proceedings of the IEEE/CVF Conference on Computer Vision and Pattern Recognition*, 2024, pp. 12385–12394.
- [14] H. B. McMahan, E. Moore, D. Ramage, S. Hampson, and B. A. y Arcas, "Communication-efficient learning of deep networks from decentralized data," in *Proceedings of the 20th International Conference on Artificial Intelligence and Statistics (AISTATS)*. PMLR, 2017, pp. 1273–1282.
- [15] H. T. Nguyen, V. Schwag, S. Hosseinalipour, C. G. Brinton, M. Chiang, and H. V. Poor, "Fast-convergent federated learning," *IEEE Journal on Selected Areas in Communications*, vol. 39, no. 1, pp. 201–218, 2020.
- [16] Y. Wang, Y. Xu, Q. Shi, and T.-H. Chang, "Quantized federated learning under transmission delay and outage constraints," *IEEE Journal on Selected Areas in Communications*, vol. 40, no. 1, pp. 323–341, 2021.
- [17] B. Luo, X. Li, S. Wang, J. Huang, and L. Tassiulas, "Cost-effective federated learning in mobile edge networks," *IEEE Journal on Selected Areas in Communications*, vol. 39, no. 12, pp. 3606–3621, 2021.
- [18] Y. Xu, B. Qian, K. Yu, T. Ma, L. Zhao, and H. Zhou, "Federated learning over fully-decoupled ran architecture for two-tier computing acceleration," *IEEE Journal on Selected Areas in Communications*, vol. 41, no. 3, pp. 789–801, 2023.
- [19] M. Chen, Z. Yang, W. Saad, C. Yin, H. V. Poor, and S. Cui, "A joint learning and communications framework for federated learning over wireless networks," *IEEE Transactions on Wireless Communications*, vol. 20, no. 1, pp. 269–283, 2020.
- [20] K. Wei, J. Li, C. Ma, M. Ding, C. Chen, S. Jin, Z. Han, and H. V. Poor, "Low-latency federated learning over wireless channels with differential privacy," *IEEE Journal on Selected Areas in Communications*, vol. 40, no. 1, pp. 290–307, 2021.
- [21] X. Yang, H. Cui, F. Dai, B. Xie, Y. He, and M. Guizani, "Communication-efficient federated learning for edge computing with gradient leakage defense," *IEEE Journal on Selected Areas in Communications*, 2025.
- [22] Z. Yang, M. Chen, W. Saad, C. S. Hong, and M. Shikh-Bahaei, "Energy efficient federated learning over wireless communication networks," *IEEE Transactions on Wireless Communications*, vol. 20, no. 3, pp. 1935–1949, 2020.
- [23] F. P.-C. Lin, S. Hosseinalipour, S. S. Azam, C. G. Brinton, and N. Michelusi, "Semi-decentralized federated learning with cooperative D2D local model aggregations," *IEEE Journal on Selected Areas in Communications*, vol. 39, no. 12, pp. 3851–3869, 2021.
- [24] W. Y. B. Lim, J. S. Ng, Z. Xiong, J. Jin, Y. Zhang, D. Niyato, C. Leung, and C. Miao, "Dynamic edge association and resource allocation in self-organizing hierarchical federated learning networks," *IEEE Journal on Selected Areas in Communications*, vol. 39, no. 12, pp. 3640–3653, 2021.
- [25] S. Luo, X. Chen, Q. Wu, Z. Zhou, and S. Yu, "HFEL: Joint edge association and resource allocation for cost-efficient hierarchical federated edge learning," *IEEE Transactions on Wireless Communications*, vol. 19, no. 10, pp. 6535–6548, 2020.
- [26] P. Yang, Y. Jiang, D. Wen, T. Wang, C. N. Jones, and Y. Shi, "Decentralized over-the-air federated learning by second-order optimization method," *IEEE Transactions on Wireless Communications*, vol. 23, no. 6, pp. 5632–5647, 2023.
- [27] H. Ye, L. Liang, and G. Y. Li, "Decentralized federated learning with unreliable communications," *IEEE Journal of Selected Topics in Signal Processing*, vol. 16, no. 3, pp. 487–500, 2022.
- [28] S. Chen, Y. Xu, H. Xu, Z. Jiang, and C. Qiao, "Decentralized federated learning with intermediate results in mobile edge computing," *IEEE Transactions on Mobile Computing*, vol. 23, no. 1, pp. 341–358, 2022.
- [29] X. Zhou, W. Liang, I. Kevin, K. Wang, Z. Yan, L. T. Yang, W. Wei, J. Ma, and Q. Jin, "Decentralized p2p federated learning for privacy-preserving and resilient mobile robotic systems," *IEEE Wireless Communications*, vol. 30, no. 2, pp. 82–89, 2023.
- [30] Y. Sun, S. Zhou, Z. Niu, and D. Gündüz, "Dynamic scheduling for over-the-air federated edge learning with energy constraints," *IEEE Journal on Selected Areas in Communications*, vol. 40, no. 1, pp. 227–242, 2021.
- [31] M. Ribero, H. Vikalo, and G. De Veciana, "Federated learning under intermittent client availability and time-varying communication constraints," *IEEE Journal of Selected Topics in Signal Processing*, vol. 17, no. 1, pp. 98–111, 2022.
- [32] Y. Ruan, X. Zhang, S.-C. Liang, and C. Joe-Wong, "Towards flexible device participation in federated learning," in *International Conference on Artificial Intelligence and Statistics*. PMLR, 2021, pp. 3403–3411.
- [33] J. Dong, L. Wang, Z. Fang, G. Sun, S. Xu, X. Wang, and Q. Zhu, "Federated class-incremental learning," in *Proceedings of the IEEE/CVF conference on computer vision and pattern recognition*, 2022, pp. 10164–10173.
- [34] J. Wang, Q. Liu, H. Liang, G. Joshi, and H. V. Poor, "Tackling the objective inconsistency problem in heterogeneous federated optimization," *Advances in neural information processing systems*, vol. 33, pp. 7611–7623, 2020.
- [35] Z.-L. Chang, D.-J. Han, S. Hosseinalipour, M. Chiang, and C. G. Brinton, "Federated learning with dynamic client arrival and departure: Convergence and rapid adaptation via initial model construction," 2025. [Online]. Available: <https://arxiv.org/abs/2410.05662>
- [36] B. Zoph, G. Ghiasi, T.-Y. Lin, Y. Cui, H. Liu, E. D. Cubuk, and Q. Le, "Rethinking pre-training and self-training," *Advances in neural information processing systems*, vol. 33, pp. 3833–3845, 2020.
- [37] T. Hsu, H. Qi, and M. Brown, "Measuring the effects of non-identical data distribution for federated visual classification," in *Proceedings of the Workshop on Federated Learning for Data Privacy and Confidentiality (NeurIPS)*, 2019.
- [38] S. Reddi, Z. Charles, M. Zaheer, Z. Garrett, K. Rush, J. Konečný, S. Kumar, and H. B. McMahan, "Adaptive federated optimization," *arXiv preprint arXiv:2003.00295*, 2020.
- [39] D. A. E. Acar, Y. Zhao, R. Matas, M. Mattina, P. Whatmough, and V. Saligrama, "Federated learning based on dynamic regularization," in *International Conference on Learning Representations*, 2021. [Online]. Available: <https://openreview.net/forum?id=B7v4QMR6Z9w>
- [40] Y. LeCun, L. Bottou, Y. Bengio, and P. Haffner, "Gradient-based learning applied to document recognition," *Proceedings of the IEEE*, vol. 86, no. 11, pp. 2278–2324, 1998.
- [41] H. Xiao, K. Rasul, and R. Vollgraf, "Fashion-mnist: a novel image dataset for benchmarking machine learning algorithms," *arXiv preprint arXiv:1708.07747*, 2017.
- [42] Y. Netzer, T. Wang, A. Coates, A. Bissacco, B. Wu, and A. Y. Ng, "Reading digits in natural images with unsupervised feature learning," *NIPS Workshop on Deep Learning and Unsupervised Feature Learning*, 2011.
- [43] A. Krizhevsky and G. Hinton, "Learning multiple layers of features from tiny images," University of Toronto, Tech. Rep., 2009.
- [44] X. Zhang, J. Zhao, and Y. LeCun, "Character-level convolutional networks for text classification," *Advances in neural information processing systems*, vol. 28, 2015.
- [45] 3rd Generation Partnership Project (3GPP), "Study on channel model for frequencies from 0.5 to 100 GHz," 3rd Generation Partnership Project (3GPP), Technical Report TR 38.901, Sep. 2025.
- [46] M. M. Amiri and D. Gündüz, "Federated learning over wireless fading channels," *IEEE Transactions on Wireless Communications*, vol. 19, no. 5, pp. 3546–3557, 2020.
- [47] N. H. Tran, W. Bao, A. Zomaya, M. N. Nguyen, and C. S. Hong, "Federated learning over wireless networks: Optimization model design and analysis," in *IEEE Conf. on Comput. Commun. (INFOCOM)*. IEEE, 2019, pp. 1387–1395.

- [48] S. L. Lohr, *Sampling: design and analysis*. Chapman and Hall/CRC, 2021.
- [49] A. Fallah, A. Mokhtari, and A. Ozdaglar, “Personalized federated learning with theoretical guarantees: A model-agnostic meta-learning approach,” in *Advances in Neural Information Processing Systems (NeurIPS)*, vol. 33, 2020, pp. 3557–3568.
- [50] Y. Le and X. Yang, “Tiny imagenet visual recognition challenge,” *CS 231N*, vol. 7, no. 7, p. 3, 2015.

APPENDIX A
COMMUNICATION AND COMPUTATION MODELING DETAILS

To evaluate the real-world performance of Algorithm 1 in a realistic wireless edge network, we model the latency and energy constraints imposed by the physical environment. We consider a Time Division Duplex (TDD) system to separate uplink and downlink transmission intervals. Within each interval, we assume an Orthogonal Frequency Division Multiple Access (OFDMA) scheme where devices are assigned orthogonal resource blocks, ensuring an interference-free environment.

A. Channel Modeling

The wireless channel between device k and the server is characterized by both large-scale and small-scale fading. The total channel gain $g_k[n]$ at time slot n is given by:

$$|g_k[n]|^2 = \psi_k \cdot |h_k[n]|^2, \quad (33)$$

where ψ_k denotes the *large-scale fading* coefficient and $h_k[n]$ represents the *small-scale fading* component.

1) *Large-Scale Fading*: We adopt the 3GPP Urban Micro (UMi) Street Canyon model defined in the technical report TR 38.901 [45], the standard for 5G/6G simulations in dense urban environments. The coefficient ψ_k captures the combined impact of path loss and shadowing. Shadowing is modeled via a random variable ξ following a zero-mean Gaussian distribution, $\xi \sim \mathcal{N}(0, \sigma_{SF}^2)$. For the UMi-LoS scenario, the standard deviation is $\sigma_{SF} = 4$ dB. The linear large-scale fading coefficient ψ_k is obtained by converting the total path loss from the logarithmic scale:

$$\psi_k = 10^{-(PL_{\text{UMi-LoS}} + \xi)/10}. \quad (34)$$

We assume ψ_k remains constant during a single communication round. The path loss $PL_{\text{UMi-LoS}}$ is divided into two segments based on a ‘‘Break Point’’ distance (d'_{BP}):

$$PL_{\text{UMi-LoS}}[\text{dB}] = \begin{cases} PL_1, & \text{if } 10\text{m} \leq d_{2D} \leq d'_{BP} \\ PL_2, & \text{if } d'_{BP} < d_{2D} \leq 5\text{km} \end{cases} \quad (35)$$

where d_{2D} is the 2D distance between the device and the Base Station (BS). The segment path losses are:

$$PL_1 = 32.4 + 21 \log_{10}(d_{3D}) + 20 \log_{10}(f_c), \quad (36)$$

$$PL_2 = 32.4 + 40 \log_{10}(d_{3D}) + 20 \log_{10}(f_c) - 9.5 \log_{10} \left((d'_{BP})^2 + (h_{\text{BS}} - h_{\text{UT}})^2 \right), \quad (37)$$

where f_c is the carrier frequency in GHz, h_{BS} is the BS height, h_{UT} is the user terminal height, and $d_{3D} = \sqrt{d_{2D}^2 + (h_{\text{BS}} - h_{\text{UT}})^2}$ is the 3D distance.

Following TR 38.901 [45], the break point distance is calculated using effective antenna heights to account for the environment height ($h_E = 1.0$ m). The effective heights are $h'_{\text{BS}} = h_{\text{BS}} - h_E$ and $h'_{\text{UT}} = h_{\text{UT}} - h_E$. Consequently, the break point distance is $d'_{BP} = (4h'_{\text{BS}}h'_{\text{UT}}f_c \times 10^9)/c$, where $c = 3 \times 10^8$ m/s.

2) *Device Distribution*: We consider a single-cell system where the server is at the center of a circular coverage area. Device locations are modeled as a Poisson Point Process (PPP) with uniform areal density within the cell, conditioned on a radius $R_{\text{cell}} = 250$ m and a minimum distance $d_{\text{min}} = 10$ m. The Euclidean 2D distance $d_{2D,k}$ of device k follows the probability density function (PDF):

$$f(d) = \frac{2d}{R_{\text{cell}}^2 - d_{\text{min}}^2}, \quad d_{\text{min}} \leq d \leq R_{\text{cell}}. \quad (38)$$

3) *Small-Scale Fading*: The factor $h_k[n]$ is modeled as a first-order time-varying Gauss-Markov process:

$$h_k[n] = \rho_k h_k[n-1] + \sqrt{1 - \rho_k^2} e_k[n], \quad (39)$$

where $e_k[n] \sim \mathcal{CN}(0, 1)$ is an i.i.d. circularly symmetric complex Gaussian random variable. The temporal correlation coefficient ρ_k is determined by the zeroth-order Bessel function of the first kind, $J_0(\cdot)$, as $\rho_k = J_0(2\pi f_d \tau)$, where τ is the slot duration and f_d is the maximum Doppler frequency, given by $f_d = v_k f_c \times 10^9/c$. To ensure the channel remains approximately constant within a slot ($\tau \ll T_c$), we calculate the coherence time $T_c \approx 0.423/f_d$ and select $\tau = 0.5$ ms.

B. Instantaneous Data Rate and Latency

Based on the TDD assumption, the *Uplink Instantaneous Data Rate* (device k to server) at time slot n is:

$$R_k^{\text{UL}}[n] = W \log_2 \left(1 + \frac{P_k^{\text{tx}} \psi_k |h_k[n]|^2}{N_0 W} \right), \quad (40)$$

where W is the channel bandwidth per device, P_k^{tx} is the transmission power of device k , and N_0 is the noise power spectral density. The *Downlink Instantaneous Data Rate* $R_k^{\text{DL}}[n]$ is calculated similarly using the server's transmission power $P_{\text{server}}^{\text{tx}}$.

The total round-trip communication latency T_k^{comm} for device k to transmit model parameters of size Z bits is:

$$T_k^{\text{comm}} = T_k^{\text{DL}} + T_k^{\text{UL}}, \quad (41)$$

where T_k^{DL} and T_k^{UL} are the minimum durations satisfying $\sum_{n=1}^{T_k^{\text{DL}}/\tau} R_k^{\text{DL}}[n] \cdot \tau \geq Z$ and $\sum_{n=1}^{T_k^{\text{UL}}/\tau} R_k^{\text{UL}}[n] \cdot \tau \geq Z$, respectively.

C. Energy Consumption and Computation

1) *Communication Energy*: The total communication energy for device k comprises the energy for receiving the global model and transmitting the local update:

$$E_k^{\text{comm}} = P_k^{\text{rx}} \cdot T_k^{\text{DL}} + P_k^{\text{tx}} \cdot T_k^{\text{UL}}, \quad (42)$$

where P_k^{rx} is the receiving circuit power. Typically $P_k^{\text{tx}} \gg P_k^{\text{rx}}$, making uplink transmission the dominant factor.

2) *Computation Latency and Energy*: Let $N_p(\mathcal{M})$ denote the number of parameters in model \mathcal{M} and $\phi(\mathcal{M})$ the computational density ratio (FLOPs/param). To account for hardware capabilities, let χ denote the processor efficiency (FLOPs/cycle). Given that device k performs $e_k^{(s,t)}$ local SGD iterations with mini-batch size $B^{(s,t)}$ during round t of session s , the local computation time T_k^{comp} is:

$$T_k^{\text{comp}} = \frac{N_p(\mathcal{M}) \cdot \phi(\mathcal{M}) \cdot e_k^{(s,t)} \cdot B^{(s,t)}}{f_k \cdot \chi}, \quad (43)$$

where f_k is the CPU clock frequency. The computation energy is modeled via the effective chipset capacitance ξ_k :

$$E_k^{\text{comp}} = \xi_k \left(\frac{N_p(\mathcal{M}) \cdot \phi(\mathcal{M}) \cdot e_k^{(s,t)} \cdot B^{(s,t)}}{\chi} \right) (f_k)^2. \quad (44)$$

APPENDIX B PROOF OF THEOREM 1

To streamline the derivation, we unify the session index $s \in \{1, \dots, S\}$ and the intra-session round index $t \in \{1, \dots, T\}$ from the main text into a single cumulative global round index $g \in \{1, \dots, G\}$, where $G = ST$. The mapping between these notations is given by $g = (s-1)T + t$. For instance, in a system where $T = 10$, the 5th round of the 3rd session ($s = 3, t = 5$) corresponds to the cumulative index $g = (3-1)10 + 5 = 25$.

Consequently, all parameters are mapped to this unified index g . For time-varying parameters such as the learning rate, we define $\eta^{(g)} \equiv \eta^{(s,t)}$. For parameters that remain constant throughout a session, such as the available device set $\mathcal{K}^{(s)}$, the notation $\mathcal{K}^{(g)}$ refers to the set associated with the unique session s containing round g (i.e., $\mathcal{K}^{(g)} \equiv \mathcal{K}^{(s)}$ holds for all g such that $\lceil g/T \rceil = s$).

Based on the local training rule and global weighted average aggregation rule, the different between two global models is

$$\mathbf{w}^{(g+1)} - \mathbf{w}^{(g)} = \sum_{k \in \mathcal{K}^{(g)}} \frac{D_k^{(g)}}{D^{(g)}} \nabla \bar{F}_k^{(g)} \quad (45)$$

where $\nabla \bar{F}_k^{(g)}$ is the accumulated gradient across $e_k^{(g)}$ local steps given by

$$\nabla \bar{F}_k^{(g)} = \left(\mathbf{w}_k^{(g), e_k^{(g)}} - \mathbf{w}^{(g)} \right) = -\eta^{(g)} \sum_{e=1}^{e_k^{(g)}} \sum_{d \in \mathcal{B}_k^{(g), e}} \frac{\nabla f(\mathbf{w}_k^{(g)}, d)}{B_k^{(g)}} \quad (46)$$

Taking the expectation of (46) and using the fact that mini-batch sampling is conducted uniformly at random without replacement, we have

$$\mathbb{E} \left[\nabla \bar{F}_k^{(g)} \right] = -\eta^{(g)} \sum_{e=1}^{e_k^{(g)}} \sum_{d \in \mathcal{D}_k^{(g)}} \frac{\nabla f(\mathbf{w}_k^{(g)}, d)}{D_k^{(g)}} \quad (47)$$

Using the β -smoothness of the global loss function Assumption (1), we have

$$F^{(g)}(\mathbf{w}^{(g+1)}) \leq F^{(g)}(\mathbf{w}^{(g)}) + \nabla F^{(g)}(\mathbf{w}^{(g)})^\top (\mathbf{w}^{(g+1)} - \mathbf{w}^{(g)}) + \frac{\beta}{2} \|\mathbf{w}^{(g+1)} - \mathbf{w}^{(g)}\|^2. \quad (48)$$

Plugging (45) and (46) into (48) and taking the expectation give

$$\begin{aligned} & \mathbb{E}_g [F^{(g)}(\mathbf{w}^{(g+1)})] \\ & \leq F^{(g)}(\mathbf{w}^{(g)}) - \eta^{(g)} \nabla F^{(g)}(\mathbf{w}^{(g)})^\top \mathbb{E}_g \left[\sum_{k \in \mathcal{K}^{(g)}} \frac{D_k^{(g)}}{D^{(g)}} \sum_{e=1}^{e_k^{(g)}} \sum_{d \in \mathcal{D}_k^{(g),e}} \frac{\nabla f(\mathbf{w}_k^{(g),e-1}, d)}{D_k^{(g)}} \right] \\ & \quad + \frac{\beta}{2} \mathbb{E}_g \left[\left\| \eta^{(g)} \sum_{k \in \mathcal{K}^{(g)}} \frac{D_k^{(g)}}{D^{(g)}} \sum_{e=1}^{e_k^{(g)}} \sum_{d \in \mathcal{B}_k^{(g),e}} \frac{\nabla f(\mathbf{w}_k^{(g),e-1}, d)}{B_k^{(g)}} \right\|^2 \right] \end{aligned} \quad (49)$$

Using the fact that for any two real-valued vectors \mathbf{a} and \mathbf{b} with the same length, we have: $2\mathbf{a}^\top \mathbf{b} = \|\mathbf{a}\|^2 + \|\mathbf{b}\|^2 - \|\mathbf{a} - \mathbf{b}\|^2$, we further obtain

$$\begin{aligned} & \mathbb{E}_g [F^{(g)}(\mathbf{w}^{(g+1)})] \leq F^{(g)}(\mathbf{w}^{(g)}) - \frac{\eta^{(g)}}{2} \sum_{k \in \mathcal{K}^{(g)}} \frac{D_k^{(g)}}{D^{(g)}} \mathbb{E}_g \left[\|\nabla F^{(g)}(\mathbf{w}^{(g)})\|^2 \right] \\ & \quad + \left\| \sum_{k \in \mathcal{K}^{(g)}} \frac{D_k^{(g)}}{D^{(g)}} \sum_{e=1}^{e_k^{(g)}} \sum_{d \in \mathcal{D}_k^{(g),e}} \frac{\nabla f(\mathbf{w}_k^{(g),e-1}, d)}{D_k^{(g)}} \right\|^2 \\ & \quad + \left\| \nabla F^{(g)}(\mathbf{w}^{(g)}) - \sum_{k \in \mathcal{K}^{(g)}} \frac{D_k^{(g)}}{D^{(g)}} \sum_{e=1}^{e_k^{(g)}} \sum_{d \in \mathcal{D}_k^{(g),e}} \frac{\nabla f(\mathbf{w}_k^{(g),e-1}, d)}{D_k^{(g)}} \right\|^2 \\ & \quad + \underbrace{\frac{\beta(\eta^{(g)})^2}{2} \mathbb{E}_g \left[\left\| \sum_{k \in \mathcal{K}^{(g)}} \frac{D_k^{(g)}}{D^{(g)}} \sum_{e=1}^{e_k^{(g)}} \sum_{d \in \mathcal{B}_k^{(g),e}} \frac{\nabla f(\mathbf{w}_k^{(g),e-1}, d)}{B_k^{(g)}} \right\|^2 \right]}_{(a)} \end{aligned} \quad (50)$$

We first bound term (a) as follows.

$$\begin{aligned} & \mathbb{E}_g \left[\left\| \sum_{k \in \mathcal{K}^{(g)}} \frac{D_k^{(g)}}{D^{(g)}} \sum_{e=1}^{e_k^{(g)}} \sum_{d \in \mathcal{B}_k^{(g),e}} \frac{\nabla f(\mathbf{w}_k^{(g),e-1}, d)}{B_k^{(g)}} \right\|^2 \right] \\ & = \mathbb{E}_g \left[\left\| \sum_{k \in \mathcal{K}^{(g)}} \frac{D_k^{(g)}}{D^{(g)}} \sum_{e=1}^{e_k^{(g)}} \left(\sum_{d \in \mathcal{B}_k^{(g),e}} \frac{\nabla f(\mathbf{w}_k^{(g),e-1}, d)}{B_k^{(g)}} - \sum_{d \in \mathcal{D}_k^{(g)}} \frac{\nabla f(\mathbf{w}_k^{(g),e-1}, d)}{D_k^{(g)}} \right) \right. \right. \\ & \quad \left. \left. + \sum_{d \in \mathcal{D}_k^{(g)}} \frac{\nabla f(\mathbf{w}_k^{(g),e-1}, d)}{D_k^{(g)}} \right\|^2 \right] \\ & \stackrel{(i)}{\leq} 2\mathbb{E}_g \left[\left\| \sum_{k \in \mathcal{K}^{(g)}} \frac{D_k^{(g)}}{D^{(g)}} \sum_{e=1}^{e_k^{(g)}} \left(\sum_{d \in \mathcal{B}_k^{(g),e}} \frac{\nabla f(\mathbf{w}_k^{(g),e-1}, d)}{B_k^{(g)}} - \sum_{d \in \mathcal{D}_k^{(g)}} \frac{\nabla f(\mathbf{w}_k^{(g),e-1}, d)}{D_k^{(g)}} \right) \right\|^2 \right] \\ & \quad + 2 \left\| \sum_{k \in \mathcal{K}^{(g)}} \frac{D_k^{(g)}}{D^{(g)}} \sum_{e=1}^{e_k^{(g)}} \sum_{d \in \mathcal{D}_k^{(g)}} \frac{\nabla f(\mathbf{w}_k^{(g),e-1}, d)}{D_k^{(g)}} \right\|^2 \\ & \stackrel{(ii)}{\leq} 2 \sum_{k \in \mathcal{K}^{(g)}} \frac{D_k^{(g)}}{D^{(g)}} \mathbb{E}_g \left[\left\| \sum_{d \in \mathcal{B}_k^{(g),e}} \frac{\nabla f(\mathbf{w}_k^{(g),e-1}, d)}{B_k^{(g)}} - \sum_{d \in \mathcal{D}_k^{(g)}} \frac{\nabla f(\mathbf{w}_k^{(g),e-1}, d)}{D_k^{(g)}} \right\|^2 \right] \end{aligned}$$

$$\begin{aligned}
& + 2 \left\| \sum_{k \in \mathcal{K}^{(g)}} \frac{D_k^{(g)}}{D^{(g)}} \sum_{e=1}^{e_k^{(g)}} \sum_{d \in \mathcal{D}_k^{(g)}} \frac{\nabla f(\mathbf{w}_k^{(g),e-1}, d)}{D_k^{(g)}} \right\|^2 \\
& \stackrel{(iii)}{\leq} 2 \sum_{k \in \mathcal{K}^{(g)}} \frac{D_k^{(g)}}{D^{(g)}} \sum_{e=1}^{e_k^{(g)}} \left(1 - \frac{B_k^{(g)}}{D_k^{(g)}} \right) \frac{(\sigma_k^{(g),e-1})^2}{B_k^{(g)}} \\
& + 2 \left\| \sum_{k \in \mathcal{K}^{(g)}} \frac{D_k^{(g)}}{D^{(g)}} \sum_{e=1}^{e_k^{(g)}} \sum_{d \in \mathcal{D}_k^{(g)}} \frac{\nabla f(\mathbf{w}_k^{(g),e-1}, d)}{D_k^{(g)}} \right\|^2.
\end{aligned} \tag{51}$$

where (i) we have used the Cauchy-Schwarz inequality $\|\mathbf{a} + \mathbf{b}\|^2 \leq 2\|\mathbf{a}\|^2 + 2\|\mathbf{b}\|^2$, (ii) we used the convex property of 2-norm, (iii) we used Eq (3.5) in chapter 3 of [48] and the definition of variance of the gradients $(\sigma_k^{(g),e-1})^2$ evaluated at the particular local step $e - 1$ for the parameter realization $\mathbf{w}_k^{(g),e-1}$. Expanding $(\sigma_k^{(g),e-1})^2$ yields

$$\begin{aligned}
& (\sigma_k^{(g),e-1})^2 \\
& = \frac{\sum_{d \in \mathcal{D}_k^{(g)}} \left\| \nabla f(\mathbf{w}_k^{(g),e-1}, d) - \frac{\sum_{d' \in \mathcal{D}_k^{(g)}} \nabla f(\mathbf{w}_k^{(g),e-1}, d')}{D_k^{(g)}} \right\|^2}{D_k^{(g)} - 1} \\
& = \frac{\sum_{d \in \mathcal{D}_k^{(g)}} \left(\frac{1}{D_k^{(g)}} \right)^2 \left\| D_k^{(g)} \nabla f(\mathbf{w}_k^{(g),e-1}, d) - \sum_{d' \in \mathcal{D}_k^{(g)}} \nabla f(\mathbf{w}_k^{(g),e-1}, d') \right\|^2}{D_k^{(g)} - 1} \\
& \stackrel{(i)}{\leq} \frac{\sum_{d \in \mathcal{D}_k^{(g)}} \frac{(D_k^{(g)} - 1)}{(D_k^{(g)})^2} \sum_{d' \in \mathcal{D}_k^{(g)}} \left\| \nabla f(\mathbf{w}_k^{(g),e-1}, d) - \nabla f(\mathbf{w}_k^{(g),e-1}, d') \right\|^2}{D_k^{(g)} - 1} \\
& \leq \frac{1}{(D_k^{(g)})^2} (\Theta^{(g)})^2 \sum_{d \in \mathcal{D}_k^{(g)}} \sum_{d' \in \mathcal{D}_k^{(g)}} \|d - d'\|^2 \\
& \leq \frac{1}{(D_k^{(g)})^2} (\Theta^{(g)})^2 \sum_{d \in \mathcal{D}_k^{(g)}} \sum_{d' \in \mathcal{D}_k^{(g)}} \|d - d'\|^2 \\
& \leq \frac{(\Theta^{(g)})^2}{(D_k^{(g)})^2} \sum_{d \in \mathcal{D}_k^{(g)}} \sum_{d' \in \mathcal{D}_k^{(g)}} \left\| d - \lambda_k^{(g)} - d' + \lambda_k^{(g)} \right\|^2 \\
& \leq \frac{(\Theta^{(g)})^2}{(D_k^{(g)})^2} \sum_{d \in \mathcal{D}_k^{(g)}} \sum_{d' \in \mathcal{D}_k^{(g)}} \left(\|d - \lambda_k^{(g)}\|^2 + \|d' - \lambda_k^{(g)}\|^2 + 2(d - \lambda_k^{(g)})^\top (d' - \lambda_k^{(g)}) \right) \\
& \stackrel{(ii)}{\leq} \frac{(\Theta^{(g)})^2}{(D_k^{(g)})^2} \left(D_k^{(g)} \sum_{d \in \mathcal{D}_k^{(g)}} \|d - \lambda_k^{(g)}\|^2 + D_k^{(g)} \sum_{d' \in \mathcal{D}_k^{(g)}} \|d' - \lambda_k^{(g)}\|^2 \right) \\
& \leq \frac{2(\Theta^{(g)})^2}{D_k^{(g)}} (\tilde{\sigma}_k^{(g)})^2.
\end{aligned} \tag{52}$$

where d denotes the feature vector of data point d , and $\lambda_k^{(g)}$ and $(\tilde{\sigma}_k^{(g)})^2$ denote the mean and sample variance of data points in $\mathcal{D}_k^{(g)}$, which are gradient independent. Also, in (i) of (52), we used the Cauchy-Schwarz inequality, and in (ii), we used the fact that $\sum_{d \in \mathcal{D}_k^{(g)}} (d - \lambda_k^{(g)}) = 0$. Plugging (52) into (51) gives

$$\begin{aligned}
& \mathbb{E}_g \left[\left\| \sum_{k \in \mathcal{K}^{(g)}} \frac{D_k^{(g)}}{D^{(g)}} \sum_{e=1}^{e_k^{(g)}} \sum_{d \in \mathcal{B}_k^{(g),e}} \frac{\nabla f(\mathbf{w}_k^{(g),e-1}, d)}{B_k^{(g),e}} \right\|^2 \right] \\
& \leq 4(\Theta^{(g)})^2 \sum_{k \in \mathcal{K}^{(g)}} \frac{D_k^{(g)}}{D^{(g)}} (\tilde{\sigma}_k^{(g)})^2 \sum_{e=1}^{e_k^{(g)}} \left(1 - \frac{B_k^{(g)}}{D_k^{(g)}} \right) \frac{1}{B_k^{(g)}}
\end{aligned}$$

$$+ 2 \left\| \sum_{k \in \mathcal{K}^{(g)}} \frac{D_k^{(g)}}{D^{(g)}} \sum_{e=1}^{e_k^{(g)}} \sum_{d \in \mathcal{D}_k^{(g)}} \frac{\nabla f(\mathbf{w}_k^{(g),e-1}, d)}{D_k^{(g)}} \right\|^2.$$

Using this, (51) becomes

$$\begin{aligned} \mathbb{E}_g [F^{(g)}(\mathbf{w}^{(g+1)})] &\leq F^{(g)}(\mathbf{w}^{(g)}) - \frac{\eta^{(g)}}{2} \sum_{k \in \mathcal{K}^{(g)}} \frac{D_k^{(g)}}{D^{(g)}} \mathbb{E}_g \left[\|\nabla F^{(g)}(\mathbf{w}^{(g)})\|^2 \right] \\ &+ \left\| \sum_{k \in \mathcal{K}^{(g)}} \frac{D_k^{(g)}}{D^{(g)}} \sum_{e=1}^{e_k^{(g)}} \sum_{d \in \mathcal{D}_k^{(g),e}} \frac{\nabla f(\mathbf{w}_k^{(g),e-1}, d)}{D_k^{(g)}} \right\|^2 \\ &+ \left\| \nabla F^{(g)}(\mathbf{w}^{(g)}) - \sum_{k \in \mathcal{K}^{(g)}} \frac{D_k^{(g)}}{D^{(g)}} \sum_{e=1}^{e_k^{(g)}} \sum_{d \in \mathcal{D}_k^{(g),e}} \frac{\nabla f(\mathbf{w}_k^{(g),e-1}, d)}{D_k^{(g)}} \right\|^2 \\ &+ 2\beta(\eta^{(g)})^2(\Theta^{(g)})^2 \sum_{k \in \mathcal{K}^{(g)}} \frac{D_k^{(g)}}{D^{(g)}} (\tilde{\sigma}_k^{(g)})^2 \sum_{e=1}^{e_k^{(g)}} \left(1 - \frac{B_k^{(g)}}{D_k^{(g)}}\right) \frac{1}{B_k^{(g)}} \\ &+ \beta(\eta^{(g)})^2 \left\| \sum_{k \in \mathcal{K}^{(g)}} \frac{D_k^{(g)}}{D^{(g)}} \sum_{e=1}^{e_k^{(g)}} \sum_{d \in \mathcal{D}_k^{(g)}} \frac{\nabla f(\mathbf{w}_k^{(g),e-1}, d)}{D_k^{(g)}} \right\|^2. \end{aligned} \quad (53)$$

Rearranging the terms, we have

$$\begin{aligned} &\mathbb{E}_g [F^{(g)}(\mathbf{w}^{(g+1)})] \\ &\leq F^{(g)}(\mathbf{w}^{(g)}) - \frac{\eta^{(g)}}{2} \sum_{k \in \mathcal{K}^{(g)}} \frac{D_k^{(g)}}{D^{(g)}} \mathbb{E}_g [\|\nabla F^{(g)}(\mathbf{w}^{(g)})\|^2] \\ &+ \left(\beta(\eta^{(g)})^2 - \frac{\eta^{(g)}}{2} \right) \sum_{k \in \mathcal{K}^{(g)}} \frac{D_k^{(g)}}{D^{(g)}} \mathbb{E}_g \left[\left\| \sum_{e=1}^{e_k^{(g)}} \sum_{d \in \mathcal{D}_k^{(g)}} \frac{\nabla f(\mathbf{w}_k^{(g),e-1}, d)}{D_k^{(g)}} \right\|^2 \right] \\ &+ \underbrace{\frac{\eta^{(g)}}{2} \sum_{k \in \mathcal{K}^{(g)}} \frac{D_k^{(g)}}{D^{(g)}} \mathbb{E}_g \left[\left\| \nabla F^{(g)}(\mathbf{w}^{(g)}) - \sum_{e=1}^{e_k^{(g)}} \sum_{d \in \mathcal{D}_k^{(g)}} \frac{\nabla f(\mathbf{w}_k^{(g),e-1}, d)}{D_k^{(g)}} \right\|^2 \right]}_{(b)} \\ &+ 2\beta(\Theta^{(g)})^2(\eta^{(g)})^2 \sum_{k \in \mathcal{K}^{(g)}} \frac{(\tilde{\sigma}_k^{(g)})^2}{D_k^{(g)}} \sum_{e=1}^{e_k^{(g)}} \left(1 - \frac{B_k^{(g)}}{D_k^{(g)}}\right) \frac{1}{B_k^{(g)}}. \end{aligned} \quad (54)$$

Term (b) in (54) can be upper bounded as

$$\begin{aligned} &\frac{\eta^{(g)}}{2} \sum_{k \in \mathcal{K}^{(g)}} \frac{D_k^{(g)}}{D^{(g)}} \mathbb{E}_g \left[\left\| \nabla F^{(g)}(\mathbf{w}^{(g)}) - \sum_{e=1}^{e_k^{(g)}} \sum_{d \in \mathcal{D}_k^{(g)}} \frac{\nabla f(\mathbf{w}_k^{(g),e-1}, d)}{D_k^{(g)}} \right\|^2 \right] \\ &= \frac{\eta^{(g)}}{2} \sum_{k \in \mathcal{K}^{(g)}} \frac{D_k^{(g)}}{D^{(g)}} \mathbb{E}_g \left[\left\| \nabla F^{(g)}(\mathbf{w}^{(g)}) - \frac{1}{e_k^{(g)}} \sum_{e=1}^{e_k^{(g)}} \sum_{d \in \mathcal{D}_k^{(g)}} \frac{\nabla f(\mathbf{w}_k^{(g),e-1}, d)}{D_k^{(g)}} \right. \right. \\ &\quad \left. \left. + \left(\frac{1}{e_k^{(g)}} - 1 \right) \sum_{e=1}^{e_k^{(g)}} \sum_{d \in \mathcal{D}_k^{(g)}} \frac{\nabla f(\mathbf{w}_k^{(g),e-1}, d)}{D_k^{(g)}} \right\|^2 \right] \\ &\leq \eta^{(g)} \sum_{k \in \mathcal{K}^{(g)}} \frac{D_k^{(g)}}{D^{(g)}} \mathbb{E}_g \left[\underbrace{\left\| \nabla F^{(g)}(\mathbf{w}^{(g)}) - \frac{1}{e_k^{(g)}} \sum_{e=1}^{e_k^{(g)}} \sum_{d \in \mathcal{D}_k^{(g)}} \frac{\nabla f(\mathbf{w}_k^{(g),e-1}, d)}{D_k^{(g)}} \right\|^2}_{(b1)} \right] \end{aligned}$$

$$+ \eta^{(g)} \left(\frac{1}{e_{\min}^{(g)}} - 1 \right)^2 \sum_{k \in \mathcal{K}^{(g)}} \frac{D_k^{(g)}}{D^{(g)}} \mathbb{E}_g \left\| \left\| \sum_{e=1}^{e_k^{(g)}} \sum_{d \in \mathcal{D}_k^{(g)}} \nabla f(\mathbf{w}_k^{(g),e-1}, d) \right\|^2 \right\|. \quad (55)$$

where $e_{\min}^{(g)} = \min_{k \in \mathcal{K}^{(g)}} e_k^{(g)}$ is the minimum number of local steps in the g -th round. Term (b1) in (55) can be upper bounded as

$$\begin{aligned} & \mathbb{E}_g \left\| \left\| \nabla F^{(g)}(\mathbf{w}^{(g)}) - \frac{1}{e_k^{(g)}} \sum_{e=1}^{e_k^{(g)}} \sum_{d \in \mathcal{D}_k^{(g)}} \frac{\nabla f(\mathbf{w}_k^{(g),e-1}, d)}{D_k^{(g)}} \right\|^2 \right\| \\ &= \mathbb{E}_g \left\| \left\| \nabla F^{(g)}(\mathbf{w}^{(g)}) - \frac{1}{e_k^{(g)}} \sum_{e=1}^{e_k^{(g)}} \nabla F_k^{(g)}(\mathbf{w}_k^{(g),e-1}) \right\|^2 \right\| \\ &\leq \sum_{k \in \mathcal{K}^{(g)}} \frac{D_k^{(g)}}{D^{(g)}} \mathbb{E}_g \left\| \left\| \nabla F_k^{(g)}(\mathbf{w}^{(g)}) - \frac{1}{e_k^{(g)}} \sum_{e=1}^{e_k^{(g)}} \nabla F_k^{(g)}(\mathbf{w}_k^{(g),e-1}) \right\|^2 \right\| \\ &\leq \sum_{k \in \mathcal{K}^{(g)}} \frac{D_k^{(g)}}{D^{(g)} e_k^{(g)}} \sum_{e=1}^{e_k^{(g)}} \mathbb{E}_g \left\| \left\| \nabla F_k^{(g)}(\mathbf{w}_k^{(g)}) - \nabla F_k^{(g)}(\mathbf{w}_k^{(g),e-1}) \right\|^2 \right\| \\ &\leq \sum_{k \in \mathcal{K}^{(g)}} \frac{D_k^{(g)}}{D^{(g)} e_k^{(g)}} \sum_{e=1}^{e_k^{(g)}} \beta^2 \mathbb{E}_g \left[\|\mathbf{w}^{(g)} - \mathbf{w}_k^{(g),e-1}\|^2 \right]. \end{aligned} \quad (56)$$

Using the local update rule, $\mathbb{E}_g \|\mathbf{w}^{(g)} - \mathbf{w}_k^{(g),e-1}\|^2$ can be further upper bounded as

$$\begin{aligned} & \mathbb{E}_g \|\mathbf{w}^{(g)} - \mathbf{w}_k^{(g),e-1}\|^2 \\ &= (\eta^{(g)})^2 \mathbb{E}_g \left\| \sum_{e'=1}^{e-1} \sum_{d \in \mathcal{B}_k^{(g),e}} \frac{\nabla f(\mathbf{w}_k^{(g),e-1}, d)}{B_k^{(g)}} \right\|^2 \\ &= (\eta^{(g)})^2 \mathbb{E}_g \left\| \sum_{e'=1}^{e-1} \left(\sum_{d \in \mathcal{B}_k^{(g),e}} \frac{\nabla f(\mathbf{w}_k^{(g),e-1}, d)}{B_k^{(g)}} - \sum_{d \in \mathcal{D}_k^{(g)}} \frac{\nabla f(\mathbf{w}_k^{(g),e-1}, d)}{D_k^{(g)}} \right. \right. \\ &\quad \left. \left. + \sum_{d \in \mathcal{D}_k^{(g)}} \frac{\nabla f(\mathbf{w}_k^{(g),e-1}, d)}{D_k^{(g)}} \right) \right\|^2 \\ &\leq 2(\eta^{(g)})^2 \mathbb{E}_g \left\| \sum_{e'=1}^{e-1} \left(\sum_{d \in \mathcal{B}_k^{(g),e}} \frac{\nabla f(\mathbf{w}_k^{(g),e-1}, d)}{B_k^{(g)}} - \sum_{d \in \mathcal{D}_k^{(g)}} \frac{\nabla f(\mathbf{w}_k^{(g),e-1}, d)}{D_k^{(g)}} \right) \right\|^2 \\ &\quad + 2(\eta^{(g)})^2 \mathbb{E}_g \left\| \sum_{e'=1}^{e-1} \sum_{d \in \mathcal{D}_k^{(g)}} \frac{\nabla f(\mathbf{w}_k^{(g),e-1}, d)}{D_k^{(g)}} \right\|^2 \\ &\leq 2(\eta^{(g)})^2 \sum_{e'=1}^{e-1} \mathbb{E}_g \left\| \sum_{d \in \mathcal{B}_k^{(g),e}} \frac{\nabla f(\mathbf{w}_k^{(g),e-1}, d)}{B_k^{(g)}} - \sum_{d \in \mathcal{D}_k^{(g)}} \frac{\nabla f(\mathbf{w}_k^{(g),e-1}, d)}{D_k^{(g)}} \right\|^2 \\ &\quad + 2(\eta^{(g)})^2 \mathbb{E}_g \left\| \sum_{e'=1}^{e-1} \sum_{d \in \mathcal{D}_k^{(g)}} \frac{\nabla f(\mathbf{w}_k^{(g),e-1}, d)}{D_k^{(g)}} \right\|^2 \\ &\leq 4(\eta^{(g)})^2 \sum_{e'=1}^{e-1} \left(1 - \frac{B_k^{(g)}}{D_k^{(g)}} \right) \frac{(\Theta^{(g)})^2}{B_k^{(g)} D_k^{(g)}} (\bar{\sigma}_k^{(g)})^2 \\ &\quad + 2(\eta^{(g)})^2 \mathbb{E}_g \left\| \sum_{e'=1}^{e-1} \sum_{d \in \mathcal{D}_k^{(g)}} \frac{\nabla f(\mathbf{w}_k^{(g),e-1}, d)}{D_k^{(g)}} \right\|^2. \end{aligned} \quad (57)$$

The last term in (57) can be further upper bounded

$$\begin{aligned}
& 2(\eta^{(g)})^2 \mathbb{E}_g \left\| \sum_{e'=1}^{e-1} \sum_{d \in \mathcal{D}_k^{(g)}} \frac{\nabla f(\mathbf{w}_k^{(g),e'-1}, d)}{D_k^{(g)}} \right\|^2 \\
& \leq 2(\eta^{(g)})^2 (e-1) \sum_{e'=1}^{e-1} \mathbb{E}_g \left\| \sum_{d \in \mathcal{D}_k^{(g)}} \frac{\nabla f(\mathbf{w}_k^{(g),e'-1}, d)}{D_k^{(g)}} \right\|^2 \\
& \leq 2(\eta^{(g)})^2 (e-1) \sum_{e'=1}^{e-1} \mathbb{E}_g \left\| \nabla F_k^{(g)}(\mathbf{w}_k^{(g),e'-1}) - \nabla F_k^{(g)}(\mathbf{w}^{(g)}) + \nabla F_k^{(g)}(\mathbf{w}^{(g)}) \right\|^2 \\
& \leq 4(\eta^{(g)})^2 (e-1) \sum_{e'=1}^{e-1} \mathbb{E}_g \left\| \nabla F_k^{(g)}(\mathbf{w}_k^{(g),e'-1}) - \nabla F_k^{(g)}(\mathbf{w}^{(g)}) \right\|^2 \\
& \quad + 4(\eta^{(g)})^2 (e-1) \sum_{e'=1}^{e-1} \left\| \nabla F_k^{(g)}(\mathbf{w}^{(g)}) \right\|^2 \\
& \leq 4\beta^2 (\eta^{(g)})^2 (e-1) \sum_{e'=1}^{e-1} \mathbb{E}_g \left\| \mathbf{w}_k^{(g),e'-1} - \mathbf{w}^{(g)} \right\|^2 \\
& \quad + 4(\eta^{(g)})^2 (e-1) \sum_{e'=1}^{e-1} \left\| \nabla F_k^{(g)}(\mathbf{w}^{(g)}) \right\|^2. \tag{58}
\end{aligned}$$

Combining (58) with (57) gives

$$\begin{aligned}
& \mathbb{E}_g \left\| \mathbf{w}^{(g)} - \mathbf{w}_k^{(g),e-1} \right\|^2 \\
& \leq 4(\eta^{(g)})^2 \sum_{e'=1}^{e-1} \left(1 - \frac{B_k^{(g)}}{D_k^{(g)}} \right) \frac{(\Theta^{(g)})^2}{B_k^{(g)} D_k^{(g)}} (\bar{\sigma}_k^{(g)})^2 \\
& \quad + 4\beta^2 (\eta^{(g)})^2 (e-1) \sum_{e'=1}^{e-1} \mathbb{E}_g \left\| \mathbf{w}_k^{(g),e'-1} - \mathbf{w}^{(g)} \right\|^2 \\
& \quad + 4(\eta^{(g)})^2 (e-1) \sum_{e'=1}^{e-1} \left\| \nabla F_k^{(g)}(\mathbf{w}^{(g)}) \right\|^2. \tag{59}
\end{aligned}$$

Taking the summation of both sides in (59) across local training steps

$$\begin{aligned}
& \sum_{e=1}^{e_k^{(g)}} \mathbb{E}_g \left\| \mathbf{w}^{(g)} - \mathbf{w}_k^{(g),e-1} \right\|^2 \\
& \leq 4(\eta^{(g)})^2 \sum_{e=1}^{e_k^{(g)}} \sum_{e'=1}^{e-1} \left(1 - \frac{B_k^{(g)}}{D_k^{(g)}} \right) \frac{(\Theta^{(g)})^2}{B_k^{(g)} D_k^{(g)}} (\bar{\sigma}_k^{(g)})^2 \\
& \quad + 4\beta^2 (\eta^{(g)})^2 \sum_{e=1}^{e_k^{(g)}} (e-1) \sum_{e'=1}^{e-1} \mathbb{E}_g \left\| \mathbf{w}_k^{(g),e'-1} - \mathbf{w}^{(g)} \right\|^2 \\
& \quad + 4(\eta^{(g)})^2 \sum_{e=1}^{e_k^{(g)}} (e-1) \sum_{e'=1}^{e-1} \left\| \nabla F_k^{(g)}(\mathbf{w}^{(g)}) \right\|^2.
\end{aligned}$$

After some simplification, we obtain

$$\begin{aligned}
& \sum_{e=1}^{e_k^{(g)}} \mathbb{E}_g \left\| \mathbf{w}^{(g)} - \mathbf{w}_k^{(g),e-1} \right\|^2 \\
& \leq 2(\eta^{(g)})^2 (e_k^{(g)} - 1) e_k^{(g)} \left(1 - \frac{B_k^{(g)}}{D_k^{(g)}} \right) \frac{(\Theta^{(g)})^2}{B_k^{(g)} D_k^{(g)}} (\bar{\sigma}_k^{(g)})^2
\end{aligned}$$

$$\begin{aligned}
& + 4\beta^2(\eta^{(g)})^2 e_k^{(g)}(e_k^{(g)} - 1) \sum_{e=1}^{e_k^{(g)}} \mathbb{E}_g \|\mathbf{w}^{(g)} - \mathbf{w}_k^{(g),e-1}\|^2 \\
& + 4(\eta^{(g)})^2 e_k^{(g)}(e_k^{(g)} - 1) \sum_{e=1}^{e_k^{(g)}} \|\nabla F_k^{(g)}(\mathbf{w}^{(g)})\|^2.
\end{aligned} \tag{60}$$

Assuming

$$\eta^{(g)} \leq \left(2\beta^2 \sqrt{e_k^{(g)}(e_k^{(g)} - 1)}\right)^{-1},$$

Performing some algebraic operations and combining the same terms on (60) gives

$$\begin{aligned}
& \sum_{e=1}^{e_k^{(g)}} \mathbb{E}_g \|\mathbf{w}^{(g)} - \mathbf{w}_k^{(g),e-1}\|^2 \\
& \leq \frac{2(\eta^{(g)})^2(e_k^{(g)} - 1)e_k^{(g)}}{1 - 4\beta^2(\eta^{(g)})^2 e_k^{(g)}(e_k^{(g)} - 1)} \left(1 - \frac{B_k^{(g)}}{D_k^{(g)}}\right) \frac{(\Theta^{(g)})^2}{B_k^{(g)} D_k^{(g)}} (\bar{\sigma}_k^{(g)})^2 \\
& + \frac{4(\eta^{(g)})^2(e_k^{(g)}(e_k^{(g)} - 1))}{1 - 4\beta^2(\eta^{(g)})^2 e_k^{(g)}(e_k^{(g)} - 1)} \sum_{e=1}^{e_k^{(g)}} \|\nabla F_k^{(g)}(\mathbf{w}^{(g)})\|^2.
\end{aligned} \tag{61}$$

Let $e_{\max}^{(g)} = \max_{k \in \mathcal{K}^{(g)}} e_k^{(g)}$ be the maximum number of local steps in the g -th round, plugging (61) in (56) gives

$$\begin{aligned}
& \mathbb{E}_g \|\nabla F^{(g)}(\mathbf{w}^{(g)}) - \frac{1}{e_k^{(g)}} \sum_{e=1}^{e_k^{(g)}} \sum_{d \in \mathcal{D}_k^{(g)}} \nabla f(\mathbf{w}_k^{(g),e-1}, d)\|^2 \\
& \leq 2(\eta^{(g)})^2 \beta^2 \sum_{k \in \mathcal{K}^{(g)}} \frac{D_k^{(g)}}{D^{(g)}} \frac{e_k^{(g)} - 1}{1 - 4\beta^2(\eta^{(g)})^2 e_k^{(g)}(e_k^{(g)} - 1)} \left(1 - \frac{B_k^{(g)}}{D_k^{(g)}}\right) \frac{(\Theta^{(g)})^2}{B_k^{(g)} D_k^{(g)}} (\bar{\sigma}_k^{(g)})^2 \\
& + \frac{4\beta^2(\eta^{(g)})^2(e_{\max}^{(g)}(e_{\max}^{(g)} - 1))}{1 - 4\beta^2(\eta^{(g)})^2 e_{\max}^{(g)}(e_{\max}^{(g)} - 1)} \sum_{k \in \mathcal{K}^{(g)}} \frac{D_k^{(g)}}{D^{(g)}} \mathbb{E}_g \|\nabla F_k^{(g)}(\mathbf{w}^{(g)})\|^2 \\
& \stackrel{(i)}{\leq} 2(\eta^{(g)})^2 \beta^2 \sum_{k \in \mathcal{K}^{(g)}} \frac{D_k^{(g)}}{D^{(g)}} \frac{e_k^{(g)} - 1}{1 - 4\beta^2(\eta^{(g)})^2 e_k^{(g)}(e_k^{(g)} - 1)} \left(1 - \frac{B_k^{(g)}}{D_k^{(g)}}\right) \frac{(\Theta^{(g)})^2}{B_k^{(g)} D_k^{(g)}} (\bar{\sigma}_k^{(g)})^2 \\
& + \frac{4\beta^2(\eta^{(g)})^2(e_{\max}^{(g)}(e_{\max}^{(g)} - 1))}{1 - 4\beta^2(\eta^{(g)})^2 e_{\max}^{(g)}(e_{\max}^{(g)} - 1)} \left(\zeta_1 \mathbb{E}_g \left\| \sum_{k \in \mathcal{K}^{(g)}} \frac{D_k^{(g)}}{D^{(g)}} \nabla F_k^{(g)}(\mathbf{w}^{(g)}) \right\|^2 + \zeta_2 \right) \\
& \leq 2(\eta^{(g)})^2 \beta^2 \sum_{k \in \mathcal{K}^{(g)}} \frac{D_k^{(g)}}{D^{(g)}} \frac{e_k^{(g)} - 1}{1 - 4\beta^2(\eta^{(g)})^2 e_k^{(g)}(e_k^{(g)} - 1)} \left(1 - \frac{B_k^{(g)}}{D_k^{(g)}}\right) \frac{(\Theta^{(g)})^2}{B_k^{(g)} D_k^{(g)}} (\bar{\sigma}_k^{(g)})^2 \\
& + \frac{4\beta^2(\eta^{(g)})^2(e_{\max}^{(g)})^2(e_{\max}^{(g)} - 1)}{1 - 4\beta^2(\eta^{(g)})^2 e_{\max}^{(g)}(e_{\max}^{(g)} - 1)} \left(\zeta_1 \mathbb{E}_g \|\nabla F^{(g)}(\mathbf{w}^{(g)})\|^2 + \zeta_2 \right).
\end{aligned} \tag{62}$$

Plugging (62) into (54) gives

$$\begin{aligned}
\mathbb{E}_g [F^{(g)}(\mathbf{w}^{(g+1)})] & \leq F^{(g)}(\mathbf{w}^{(g)}) + 2\beta(\Theta^{(g)})^2(\eta^{(g)})^2 \sum_{k \in \mathcal{K}^{(g)}} \frac{(\bar{\sigma}_k^{(g)})^2}{D_k^{(g)}} \sum_{e=1}^{e_k^{(g)}} \left(1 - \frac{B_k^{(g)}}{D_k^{(g)}}\right) \frac{1}{B_k^{(g)}} \\
& + (\eta^{(g)})^3 \beta^2 \sum_{k \in \mathcal{K}^{(g)}} \frac{D_k^{(g)}}{D^{(g)}} \frac{e_k^{(g)} - 1}{1 - 4\beta^2(\eta^{(g)})^2 e_k^{(g)}(e_k^{(g)} - 1)} \left(1 - \frac{B_k^{(g)}}{D_k^{(g)}}\right) \frac{(\Theta^{(g)})^2}{B_k^{(g)} D_k^{(g)}} (\bar{\sigma}_k^{(g)})^2 \\
& + \underbrace{\left(\beta(\eta^{(g)})^2 - \frac{\eta^{(g)}}{2} + \eta^{(g)} \left(\frac{1}{e_{\min}^{(g)}} - 1 \right) \right)}_{(c)} \sum_{k \in \mathcal{K}^{(g)}} \frac{D_k^{(g)}}{D^{(g)}} \mathbb{E}_g \left\| \sum_{e=1}^{e_k^{(g)}} \sum_{d \in \mathcal{D}_k^{(g)}} \frac{\nabla f(\mathbf{w}_k^{(g),e-1}, d)}{D_k^{(g)}} \right\|^2
\end{aligned}$$

$$\begin{aligned}
& + \frac{2\beta^2(\eta^{(g)})^3(e_{\max}^{(g)})^2(e_{\max}^{(g)} - 1)}{1 - 4\beta^2(\eta^{(g)})^2 e_{\max}^{(g)}(e_{\max}^{(g)} - 1)} \zeta_2 \\
& + \frac{\eta^{(g)}}{2} \left(\frac{4\beta^2(\eta^{(g)})^2(e_{\max}^{(g)})^2(e_{\max}^{(g)} - 1)}{1 - 4\beta^2(\eta^{(g)})^2 e_{\max}^{(g)}(e_{\max}^{(g)} - 1)} \zeta_1 - 1 \right) \left\| \nabla F^{(g)}(\mathbf{w}^{(g)}) \right\|^2.
\end{aligned} \tag{63}$$

To eliminate term (c) in (63), we need to make

$$\beta(\eta^{(g)})^2 - \frac{\eta^{(g)}}{2} + \eta^{(g)} \left(\frac{1}{e_{\min}^{(g)}} - 1 \right)^2 < 0, \tag{64}$$

we require

$$\eta^{(g)} < \left(\frac{1}{2} - \left(\frac{1}{e_{\min}^{(g)}} - 1 \right)^2 \right) \frac{1}{\beta}. \tag{65}$$

Also, we aim to make

$$\frac{4\beta^2(\eta^{(g)})^2(e_{\max}^{(g)})^2(e_{\max}^{(g)} - 1)}{1 - 4\beta^2(\eta^{(g)})^2 e_{\max}^{(g)}(e_{\max}^{(g)} - 1)} - 1 < 0. \tag{66}$$

$$1 - 4\beta^2(\eta^{(g)})^2 e_{\max}^{(g)}(e_{\max}^{(g)} - 1) > 0. \tag{67}$$

Thus, we get the condition:

$$\eta^{(g)} < \frac{1}{2\beta\sqrt{e_{\max}^{(g)}(e_{\max}^{(g)} - 1)}}. \tag{68}$$

Assume there exists a set of constants $\Lambda^{(g)}$, $\forall g$, where:

$$\frac{4(\eta^{(g)})^2\beta^2(\Theta^{(g)})^2(e_{\max}^{(g)}(e_{\max}^{(g)} - 1))}{1 - 4(\eta^{(g)})^2\beta^2 e_{\max}^{(g)}(e_{\max}^{(g)} - 1)} \zeta_1 < \Lambda^{(g)} < 1, \quad \Lambda^{(g)} < \zeta_1 \tag{69}$$

Then we will have

$$\eta^{(g)} \leq \frac{\sqrt{\Lambda^{(g)}}}{2\beta\sqrt{(\zeta_1 + \Lambda^{(g)})e_{\max}^{(g)}(e_{\max}^{(g)} - 1)}} \tag{70}$$

and

$$\frac{1}{(1 - 4(\eta^{(g)})^2\beta^2 e_{\max}^{(g)}(e_{\max}^{(g)} - 1))} \leq \frac{\zeta_1 + \Lambda^{(g)}}{\zeta_1} \tag{71}$$

Note that the condition in (70) is stricter than (68). Putting altogether, we get

$$\begin{aligned}
& \|\nabla F^{(g)}(\mathbf{w}^{(g)})\|^2 \\
& \leq \frac{2(F^{(g)}(\mathbf{w}^{(g)}) - \mathbb{E}_g[F^{(g)}(\mathbf{w}^{(g+1)})])}{\eta^{(g)}(1 - \Lambda^{(g)})} \\
& + \frac{4\beta(\Theta^{(g)})^2\eta^{(g)}}{1 - \Lambda^{(g)}} \sum_{k \in \mathcal{K}^{(g)}} \frac{(\tilde{\sigma}_k^{(g)})^2}{D_k^{(g)}} e_k^{(g)} \left(1 - \frac{B_k^{(g)}}{D_k^{(g)}} \right) \frac{1}{B_k^{(g)}} \\
& + \frac{2\beta^2(\eta^{(g)})^2}{D^{(g)}(1 - \Lambda^{(g)})} \sum_{k \in \mathcal{K}^{(g)}} (e_k^{(g)} - 1) \frac{\zeta_1 + \Lambda^{(g)}}{\zeta_1} \left(1 - \frac{B_k^{(g)}}{D_k^{(g)}} \right) \frac{(\Theta^{(g)})(\tilde{\sigma}_k^{(g)})^2}{B_k^{(g)}} \\
& + 4\beta^2(\eta^{(g)})^2(e_{\max}^{(g)})(e_{\max}^{(g)} - 1) \frac{\zeta_2}{1 - \Lambda^{(g)}} \frac{(\zeta_1 + \Lambda^{(g)})}{\zeta_1}
\end{aligned}$$

Summing from 1 to G and dividing by G and applying $\frac{\zeta_1 + \Lambda^{(g)}}{\zeta_1} < 2$ lead to

$$\frac{1}{G} \sum_{g=1}^G \|\nabla F^{(g)}(\mathbf{w}^{(g)})\|^2$$

$$\begin{aligned}
&\leq \frac{1}{G} \sum_{g=1}^G \frac{2(F^{(g)}(\mathbf{w}^{(g)}) - \mathbb{E}_g[F^{(g)}(\mathbf{w}^{(g+1)})])}{\eta^{(g)}(1 - \Lambda^{(g)})} \\
&\quad + \frac{1}{G} \sum_{g=1}^G \frac{4\beta(\Theta^{(g)})^2(\eta^{(g)})}{1 - \Lambda^{(g)}} \sum_{k \in \mathcal{K}^{(g)}} \frac{(\tilde{\sigma}_k^{(g)})^2}{D_k^{(g)}} e_k^{(g)} \left(1 - \frac{B_k^{(g)}}{D_k^{(g)}}\right) \frac{1}{B_k^{(g)}} \\
&\quad + \frac{1}{G} \sum_{g=1}^G \frac{4\beta^2(\eta^{(g)})^2}{D^{(g)}(1 - \Lambda^{(g)})} \sum_{k \in \mathcal{K}^{(g)}} (e_k^{(g)} - 1) \left(1 - \frac{B_k^{(g)}}{D_k^{(g)}}\right) \frac{(\Theta^{(g)})(\tilde{\sigma}_k^{(g)})^2}{B_k^{(g)}} \\
&\quad + \frac{1}{G} \sum_{g=1}^G 8\beta^2(\eta^{(g)})^2 (e_{\max}^{(g)})(e_{\max}^{(g)} - 1) \frac{\zeta_2}{1 - \Lambda^{(g)}}
\end{aligned}$$

APPENDIX C

EXPERIMENTAL SETUP, REPRODUCIBILITY, AND COMPUTATIONAL RESOURCES

A. Setup and Reproducibility

The following command was used to launch each experiment. The meaning and purpose of each argument are described in detail in our accompanying README.md.

```
python -u fasy_adapt_training.py \
  --dataset_name 'cifar10' \
  --algorithm 'scaffold' \
  --cross_session_label_overlap 0.0 \
  --in_session_label_dist "dirichlet" \
  --dirichlet_alpha 0.7 \
  --seed 300 \
  --initial 1 \
  --average 1 \
  --previous 1 \
  --continuous 0 \
  --num_clients 100 \
  --num_sessions 7 \
  --num_sessions_pilot 1 \
  --num_rounds_pilot 100 \
  --num_rounds_actual 100 \
  --lr_config_path 'lr_poly.json' \
  --momentum 0.9 \
  --gpu_index 0 \
  --num_SGD_training 5 \
  --batch_size_training 128 \
  --num_SGD_grad_cal 5 \
  --batch_size_grad_cal 128 \
  --prox_alpha 1.0 \
  --moon_mu 1.0 \
  --moon_tau 1.0 \
  --kl_coefficient 0.5 \
  --acg_beta 0.1 \
  --acg_lambda 0.5 \
  --num_round_grad_cal 1 \
  --similarity "two_norm" \
  --similarity_scale 10.0
```

B. How hyperparameters were chosen

The parameter *num_sessions* must be at least two greater than *num_sessions_pilot* to observe the effect of our proposed scheme. The parameters *num_rounds_pilot*, *num_rounds_actual*, *num_SGD_training*, *num_SGD_grad_cal*, and *num_round_grad_cal* all take positive integer values, while *similarity_scale* is a positive real number. We experimented with values such as 10, 100, 500, and 800, and selected appropriate settings based on the model and dataset. In principle, most

hyperparameters were chosen such that training within each session converges by its final round, using the smallest values possible to ensure fair comparison across algorithms and datasets.

Algorithm-specific parameters include $prox_alpha$, $moon_mu$, $moon_tau$, $kl_coefficient$, acg_beta , and acg_lambda . These were selected based on the model architecture, data distribution, and dataset characteristics, or by following the recommended values from the respective original papers.

C. Baseline variants:

AG News uses the average and previous baselines. All other datasets use average, previous, and continuous baselines.

100 Clients Configuration

- $num_sessions=7$
- $acg_beta=0.1, acg_lambda=0.5$
- Algorithms:
 - All datasets: MOON ($moon_mu=1.0, moon_tau=1.0$), FedProx ($prox_alpha=1.0$), SCAFFOLD, FedACG
- $kl_coefficient = 1.0$ for all datasets except AG News (0.5)
- $similarity_scale = 10.0$ for image datasets; AG News uses 800
- Random seeds: 100, 200, 300

Training Rounds (all clients)

- MNIST, Fashion-MNIST: 50 pilot rounds, 50 actual rounds
- SVHN, TinyImageNet: 200 pilot rounds, 200 actual rounds
- CIFAR-10, CIFAR-100: 150 pilot rounds, 150 actual rounds
- AG News: 100 pilot rounds, 100 actual rounds

Shared Parameters Across All Experiments

- $momentum=0.9$
- $num_SGD_training=5, batch_size_training=128$
- $num_SGD_grad_cal=5, batch_size_grad_cal=128$
- $num_round_grad_cal=1$
- Learning rate scheduler: $lr_config_path = 'lr_poly.json'$

D. Compute Resources

All experiments were conducted on a high-performance node provided by our university’s Advanced Computing Center, equipped with two Intel Xeon Platinum 8480+ 56-core CPUs (3.8 GHz), eight NVIDIA H100 GPUs (80 GB each), and 1031 GB of RAM. Each SLURM job was allocated one H100 GPU and 14 CPU cores.

Table VIII presents a comprehensive overview of average CPU time and maximum memory usage for our experiments with 20 clients. The average is taken over three random seeds.

TABLE VIII: Average CPU time and average maximum memory usage across three random seeds for our experiments with 20 clients.

Dataset	Cross	Alpha	Method	CPU Time	Max Mem
MNIST	0.2	0.3	FedAvg	00:26:28	1.07G
MNIST	0.2	0.3	FedProx	00:26:33	1.11G
MNIST	0.2	0.3	SCAFFOLD	00:26:19	1.06G
MNIST	0.2	0.3	FedACG	00:26:18	1.10G
MNIST	0.2	0.7	FedAvg	00:25:51	1.06G
MNIST	0.2	0.7	FedProx	00:26:00	1.11G
MNIST	0.2	0.7	SCAFFOLD	00:25:45	1.05G
MNIST	0.2	0.7	FedACG	00:26:09	1.11G
MNIST	0.0	0.3	FedAvg	00:26:04	1.05G
MNIST	0.0	0.3	FedProx	00:26:13	1.12G

Continued on next page

Dataset	Cross Vals	Alpha Vals	Method	CPU Time	Max Mem
MNIST	0.0	0.3	SCAFFOLD	00:25:49	1.06G
MNIST	0.0	0.3	FedACG	00:25:53	1.10G
MNIST	0.0	0.7	FedAvg	00:26:08	1.06G
MNIST	0.0	0.7	FedProx	00:17:36	1.07G
MNIST	0.0	0.7	SCAFFOLD	00:17:29	1.03G
MNIST	0.0	0.7	FedACG	00:18:04	1.07G
FMNIST	0.2	0.3	FedAvg	00:25:52	1.10G
FMNIST	0.2	0.3	FedProx	00:26:09	1.14G
FMNIST	0.2	0.3	SCAFFOLD	00:25:58	1.07G
FMNIST	0.2	0.3	FedACG	00:26:18	1.13G
FMNIST	0.2	0.7	FedAvg	00:25:42	1.07G
FMNIST	0.2	0.7	FedProx	00:26:24	1.09G
FMNIST	0.2	0.7	SCAFFOLD	00:26:22	1.06G
FMNIST	0.2	0.7	FedACG	00:25:55	1.10G
FMNIST	0.0	0.3	FedAvg	00:25:50	1.08G
FMNIST	0.0	0.3	FedProx	00:26:28	1.10G
FMNIST	0.0	0.3	SCAFFOLD	00:26:10	1.06G
FMNIST	0.0	0.3	FedACG	00:26:25	1.11G
FMNIST	0.0	0.7	FedAvg	00:25:53	1.07G
FMNIST	0.0	0.7	FedProx	00:26:22	1.10G
FMNIST	0.0	0.7	SCAFFOLD	00:25:38	1.07G
FMNIST	0.0	0.7	FedACG	00:26:21	1.11G
SVHN	0.2	0.3	FedAvg	03:58:13	2.70G
SVHN	0.2	0.3	FedProx	04:14:29	2.74G
SVHN	0.2	0.3	SCAFFOLD	04:11:40	2.59G
SVHN	0.2	0.3	FedACG	04:16:08	2.46G
SVHN	0.2	0.7	FedAvg	04:01:22	2.69G
SVHN	0.2	0.7	FedProx	04:07:41	2.72G
SVHN	0.2	0.7	SCAFFOLD	04:01:41	2.57G
SVHN	0.2	0.7	FedACG	04:14:45	2.46G
SVHN	0.0	0.3	FedAvg	03:53:31	2.69G
SVHN	0.0	0.3	FedProx	04:03:16	2.72G
SVHN	0.0	0.3	SCAFFOLD	03:58:43	2.56G
SVHN	0.0	0.3	FedACG	04:04:32	2.42G
SVHN	0.0	0.7	FedAvg	03:57:38	2.67G
SVHN	0.0	0.7	FedProx	04:10:49	2.73G
SVHN	0.0	0.7	SCAFFOLD	04:00:49	2.57G
SVHN	0.0	0.7	FedACG	04:04:58	2.42G
CIFAR-10	0.2	0.3	FedAvg	04:48:29	13.67G
CIFAR-10	0.2	0.3	FedProx	05:22:40	13.74G
CIFAR-10	0.2	0.3	SCAFFOLD	06:30:16	14.68G
CIFAR-10	0.2	0.3	FedACG	05:51:08	13.33G
CIFAR-10	0.2	0.7	FedAvg	04:55:07	13.62G
CIFAR-10	0.2	0.7	FedProx	05:27:18	13.69G
CIFAR-10	0.2	0.7	SCAFFOLD	06:30:14	14.54G
CIFAR-10	0.2	0.7	FedACG	05:50:24	13.34G
CIFAR-10	0.0	0.3	FedAvg	04:55:51	13.65G
CIFAR-10	0.0	0.3	FedProx	05:31:49	13.72G
CIFAR-10	0.0	0.3	SCAFFOLD	06:33:56	14.55G
CIFAR-10	0.0	0.3	FedACG	05:51:33	13.35G

Continued on next page

Dataset	Cross Vals	Alpha Vals	Method	CPU Time	Max Mem
CIFAR-10	0.0	0.7	FedAvg	04:59:05	13.64G
CIFAR-10	0.0	0.7	FedProx	05:18:14	13.72G
CIFAR-10	0.0	0.7	SCAFFOLD	06:30:40	14.67G
CIFAR-10	0.0	0.7	FedACG	05:40:13	13.38G
CIFAR-100	0.2	0.3	FedAvg	05:07:17	13.66G
CIFAR-100	0.2	0.3	FedProx	05:27:38	13.78G
CIFAR-100	0.2	0.3	SCAFFOLD	06:34:27	14.61G
CIFAR-100	0.2	0.3	FedACG	05:45:00	13.22G
CIFAR-100	0.2	0.7	FedAvg	05:04:29	13.73G
CIFAR-100	0.2	0.7	FedProx	05:29:20	13.78G
CIFAR-100	0.2	0.7	SCAFFOLD	06:29:29	14.65G
CIFAR-100	0.2	0.7	FedACG	05:45:25	13.26G
CIFAR-100	0.0	0.3	FedAvg	04:53:37	13.71G
CIFAR-100	0.0	0.3	FedProx	05:25:04	13.82G
CIFAR-100	0.0	0.3	SCAFFOLD	06:30:22	14.56G
CIFAR-100	0.0	0.3	FedACG	05:43:58	13.24G
CIFAR-100	0.0	0.7	FedAvg	04:55:26	13.71G
CIFAR-100	0.0	0.7	FedProx	05:14:38	13.76G
CIFAR-100	0.0	0.7	SCAFFOLD	06:21:14	14.69G
CIFAR-100	0.0	0.7	FedACG	05:38:40	13.25G
TinyImageNet	0.2	0.3	MOON	18:39:30	26.12G
TinyImageNet	0.2	0.3	FedProx	16:22:46	25.01G
TinyImageNet	0.2	0.3	FedACG	17:02:45	23.38G
TinyImageNet	0.2	0.7	MOON	18:08:26	26.20G
TinyImageNet	0.2	0.7	FedProx	15:49:21	25.03G
TinyImageNet	0.2	0.7	FedACG	16:46:22	23.43G
TinyImageNet	0.0	0.3	MOON	18:09:04	26.17G
TinyImageNet	0.0	0.3	FedProx	15:22:17	25.12G
TinyImageNet	0.0	0.3	FedACG	16:31:42	23.34G
TinyImageNet	0.0	0.7	MOON	17:56:09	26.09G
TinyImageNet	0.0	0.7	FedProx	15:59:06	25.02G
TinyImageNet	0.0	0.7	FedACG	16:40:21	23.27G
AG News	0.8	0.3	FedAvg	01:04:40	9.97G
AG News	0.8	0.3	FedProx	01:05:43	10.02G
AG News	0.8	0.3	SCAFFOLD	02:29:40	8.61G
AG News	0.8	0.3	FedACG	01:19:28	8.62G
AG News	0.8	0.7	FedAvg	01:03:21	9.96G
AG News	0.8	0.7	FedProx	01:05:03	9.99G
AG News	0.8	0.7	SCAFFOLD	02:29:45	8.62G
AG News	0.8	0.7	FedACG	01:16:25	8.62G
AG News	0.0	0.3	FedAvg	01:02:22	9.98G
AG News	0.0	0.3	FedProx	01:03:02	9.99G
AG News	0.0	0.3	SCAFFOLD	02:27:12	8.59G
AG News	0.0	0.3	FedACG	01:15:39	8.67G
AG News	0.0	0.7	FedAvg	01:00:31	9.96G
AG News	0.0	0.7	FedProx	01:04:21	10.00G
AG News	0.0	0.7	SCAFFOLD	02:28:45	8.64G
AG News	0.0	0.7	FedACG	01:13:27	8.65G

Table IX presents a comprehensive overview of average CPU time and average maximum memory usage for our experiments

with 100 clients. The average is taken over three random seeds.

TABLE IX: Average CPU time and average maximum memory usage across three random seeds for our experiments with 100 clients.

Dataset	Cross	Alpha	Method	CPU Time	Max Mem
MNIST	0.2	0.3	MOON	00:59:59	1.29G
MNIST	0.2	0.3	FedProx	00:57:34	1.17G
MNIST	0.2	0.3	SCAFFOLD	00:56:08	1.11G
MNIST	0.2	0.3	FedACG	00:57:24	1.16G
MNIST	0.2	0.7	MOON	00:59:29	1.29G
MNIST	0.2	0.7	FedProx	00:57:02	1.17G
MNIST	0.2	0.7	SCAFFOLD	00:55:34	1.13G
MNIST	0.2	0.7	FedACG	00:56:42	1.15G
MNIST	0.0	0.3	MOON	00:59:09	1.28G
MNIST	0.0	0.3	FedProx	00:58:24	1.15G
MNIST	0.0	0.3	SCAFFOLD	00:56:19	1.13G
MNIST	0.0	0.3	FedACG	00:57:24	1.14G
MNIST	0.0	0.7	MOON	01:00:03	1.27G
MNIST	0.0	0.7	FedProx	00:58:13	1.16G
MNIST	0.0	0.7	SCAFFOLD	00:55:47	1.12G
MNIST	0.0	0.7	FedACG	00:57:15	1.17G
FMNIST	0.2	0.3	MOON	00:59:49	1.27G
FMNIST	0.2	0.3	FedProx	00:57:43	1.15G
FMNIST	0.2	0.3	SCAFFOLD	00:55:53	1.13G
FMNIST	0.2	0.3	FedACG	00:57:33	1.16G
FMNIST	0.2	0.7	MOON	00:59:47	1.29G
FMNIST	0.2	0.7	FedProx	00:57:40	1.16G
FMNIST	0.2	0.7	SCAFFOLD	00:56:19	1.11G
FMNIST	0.2	0.7	FedACG	00:57:41	1.16G
FMNIST	0.0	0.3	MOON	00:59:55	1.28G
FMNIST	0.0	0.3	FedProx	00:56:43	1.17G
FMNIST	0.0	0.3	SCAFFOLD	00:56:31	1.13G
FMNIST	0.0	0.3	FedACG	00:57:57	1.17G
FMNIST	0.0	0.7	MOON	00:59:52	1.27G
FMNIST	0.0	0.7	FedProx	00:58:14	1.16G
FMNIST	0.0	0.7	SCAFFOLD	00:56:14	1.12G
FMNIST	0.0	0.7	FedACG	00:57:09	1.15G
SVHN	0.2	0.3	MOON	11:38:02	6.44G
SVHN	0.2	0.3	FedProx	10:38:06	5.99G
SVHN	0.2	0.3	SCAFFOLD	10:29:37	5.85G
SVHN	0.2	0.3	FedACG	10:55:30	5.17G
SVHN	0.2	0.7	MOON	12:11:57	6.42G
SVHN	0.2	0.7	FedProx	11:14:06	6.09G
SVHN	0.2	0.7	SCAFFOLD	11:04:21	5.84G
SVHN	0.2	0.7	FedACG	10:56:34	5.17G
SVHN	0.0	0.3	MOON	11:50:13	6.48G
SVHN	0.0	0.3	FedProx	10:22:12	6.06G
SVHN	0.0	0.3	SCAFFOLD	10:14:38	5.96G
SVHN	0.0	0.3	FedACG	10:51:27	5.23G
SVHN	0.0	0.7	MOON	11:32:17	6.47G

Continued on next page

Dataset	Cross Vals	Alpha Vals	Method	CPU Time	Max Mem
SVHN	0.0	0.7	FedProx	11:03:23	6.09G
SVHN	0.0	0.7	SCAFFOLD	10:50:04	5.77G
SVHN	0.0	0.7	FedACG	10:36:18	5.19G
CIFAR-10	0.2	0.3	MOON	16:52:19	61.25G
CIFAR-10	0.2	0.3	FedProx	12:59:18	57.32G
CIFAR-10	0.2	0.3	SCAFFOLD	20:22:25	56.64G
CIFAR-10	0.2	0.3	FedACG	14:38:38	53.22G
CIFAR-10	0.2	0.7	MOON	17:31:36	61.08G
CIFAR-10	0.2	0.7	FedProx	13:19:24	57.28G
CIFAR-10	0.2	0.7	SCAFFOLD	20:15:41	56.52G
CIFAR-10	0.2	0.7	FedACG	14:25:16	53.29G
CIFAR-10	0.0	0.3	MOON	17:20:51	61.31G
CIFAR-10	0.0	0.3	FedProx	13:24:55	57.27G
CIFAR-10	0.0	0.3	SCAFFOLD	20:25:56	56.51G
CIFAR-10	0.0	0.3	FedACG	14:48:45	53.14G
CIFAR-10	0.0	0.7	MOON	17:26:10	61.26G
CIFAR-10	0.0	0.7	FedProx	13:23:31	57.17G
CIFAR-10	0.0	0.7	SCAFFOLD	20:03:12	56.40G
CIFAR-10	0.0	0.7	FedACG	14:50:02	53.19G
CIFAR-100	0.2	0.3	MOON	19:23:54	62.38G
CIFAR-100	0.2	0.3	FedProx	14:53:36	57.47G
CIFAR-100	0.2	0.3	SCAFFOLD	21:45:50	58.21G
CIFAR-100	0.2	0.3	FedACG	16:31:56	54.33G
CIFAR-100	0.2	0.7	MOON	19:05:52	62.30G
CIFAR-100	0.2	0.7	FedProx	14:58:14	57.43G
CIFAR-100	0.2	0.7	SCAFFOLD	21:39:22	58.15G
CIFAR-100	0.2	0.7	FedACG	16:18:23	54.22G
CIFAR-100	0.0	0.3	MOON	17:36:12	62.01G
CIFAR-100	0.0	0.3	FedProx	13:27:23	57.11G
CIFAR-100	0.0	0.3	SCAFFOLD	20:51:50	58.11G
CIFAR-100	0.0	0.3	FedACG	15:04:23	54.19G
CIFAR-100	0.0	0.7	MOON	17:43:03	62.00G
CIFAR-100	0.0	0.7	FedProx	13:26:15	57.19G
CIFAR-100	0.0	0.7	SCAFFOLD	20:09:42	58.26G
CIFAR-100	0.0	0.7	FedACG	14:50:34	54.36G
AG News	0.8	0.3	MOON	07:28:40	39.48G
AG News	0.8	0.3	FedProx	05:05:26	42.81G
AG News	0.8	0.3	SCAFFOLD	10:45:28	31.41G
AG News	0.8	0.3	FedACG	06:12:14	35.95G
AG News	0.8	0.7	MOON	07:26:40	39.39G
AG News	0.8	0.7	FedProx	05:14:55	42.77G
AG News	0.8	0.7	SCAFFOLD	11:04:57	31.39G
AG News	0.8	0.7	FedACG	06:02:33	35.95G
AG News	0.0	0.3	MOON	07:28:01	39.42G
AG News	0.0	0.3	FedProx	04:59:05	42.79G
AG News	0.0	0.3	SCAFFOLD	11:25:17	33.66G
AG News	0.0	0.3	FedACG	05:49:40	35.98G
AG News	0.0	0.7	MOON	07:29:04	39.55G
AG News	0.0	0.7	FedProx	05:11:57	42.84G
AG News	0.0	0.7	SCAFFOLD	10:57:00	31.42G

Continued on next page

Dataset	Cross Vals	Alpha Vals	Method	CPU Time	Max Mem
AG News	0.0	0.7	FedACG	05:51:58	36.01G
Tinyimagenet	0.2	0.3	MOON	71:04:06	107.02G
Tinyimagenet	0.2	0.3	FedProx	60:05:53	104.66G
Tinyimagenet	0.2	0.3	SCAFFOLD	72:56:11	95.09G
Tinyimagenet	0.2	0.3	FedACG	63:35:32	92.64G
Tinyimagenet	0.2	0.7	MOON	77:32:22	106.88G
Tinyimagenet	0.2	0.7	FedProx	64:33:53	104.34G
Tinyimagenet	0.2	0.7	SCAFFOLD	79:16:25	94.82G
Tinyimagenet	0.2	0.7	FedACG	66:31:58	92.48G
Tinyimagenet	0.0	0.3	MOON	70:13:51	106.77G
Tinyimagenet	0.0	0.3	FedProx	58:26:32	104.38G
Tinyimagenet	0.0	0.3	SCAFFOLD	73:27:39	95.02G
Tinyimagenet	0.0	0.3	FedACG	61:50:21	92.33G
Tinyimagenet	0.0	0.7	MOON	69:09:45	106.72G
Tinyimagenet	0.0	0.7	FedProx	59:04:02	104.18G
Tinyimagenet	0.0	0.7	SCAFFOLD	71:57:32	95.24G
Tinyimagenet	0.0	0.7	FedACG	61:02:40	92.33G

APPENDIX D

SUPPLEMENTARY RESULTS ON LABEL DISTRIBUTIONS FROM THE MAIN TEXT

Tables X further demonstrates the effectiveness of Algorithm 1 on the MNIST, Fashion-MNIST, SVHN, CIFAR-10, and CIFAR-100 datasets with 100 clients.

APPENDIX E

ADDITIONAL RESULTS FOR ALTERNATIVE LABEL DISTRIBUTIONS

In addition to the label distribution we used in the main text, we also evaluate Algorithm 1 using the following distribution.

- **Two-Shard** [9], [10], [14], [37], [49]: For datasets with 10 labels, each label is divided into two equally-sized shards, and each client receives two different label shards. For datasets with 100 labels, the labels are divided into 10 non-overlapping batches, and each batch is split into two shards, which are then assigned to two randomly selected clients. Each client ends up with data from two labels for 10-label datasets, or 20 labels for 100-label datasets .
- **Half**: Half the clients have one half of the labels, and the rest have the other half. Each client has all the labels from their assigned half (i.e., 5 labels for 10-label datasets or 50 labels for 100-label datasets), and the data is evenly distributed, meaning that the amount of data for each label is equally divided among the clients.
- **Partial-Overlap**: Two sets of labels are selected, each containing 60% of the total labels, with a 20% overlap between them. Each client in the first set has 6 labels for 10-label datasets (or 60 labels for 100-label datasets), and each client in the second set has a similar distribution. The overlapping labels are split between the two halves of clients, with half of the data for overlapping labels going to the first client set and the other half to the second set. The non-overlapping labels are assigned to the clients within each set, and the data corresponding to these labels is evenly distributed across the clients, meaning that each client receives an approximately equal share of the data for their assigned labels.
- **Distinct**: Each client is assigned a unique set of labels. For datasets with 10 labels, each client receives 1 unique label, while for datasets with 100 labels, each client receives 10 unique labels.

Figure 5 highlights selected scenarios and illustrates the advantages of the proposed algorithm for all FL algorithms during periods of pronounced performance drops or gains due to data distribution shifts. The algorithm prioritizes models trained on past distributions similar to the current one, enabling the initial model to adapt more quickly and consistently outperform baseline approaches. These results underscore the robustness and effectiveness of the proposed approach across diverse FL algorithms, datasets, models, and dynamic data distributions.

Table XI compares the average accuracy of the proposed algorithm across all FL algorithms during the first 10 global rounds after three data distribution shifts under the “Two-Shard” and “Partial-Overlap” label distributions. The results across datasets, label distributions, and models show that the proposed algorithm mitigates performance degradation from dynamic client arrivals and departures. Moreover, it accelerates performance recovery when the current data distribution aligns with a previously observed one.

Table XII presents a comparative analysis of the average accuracy achieved by the proposed algorithm across all federated learning (FL) algorithms during the first 10 global rounds following three shifts in data distribution under the “Half” and “Distinct” label distributions.

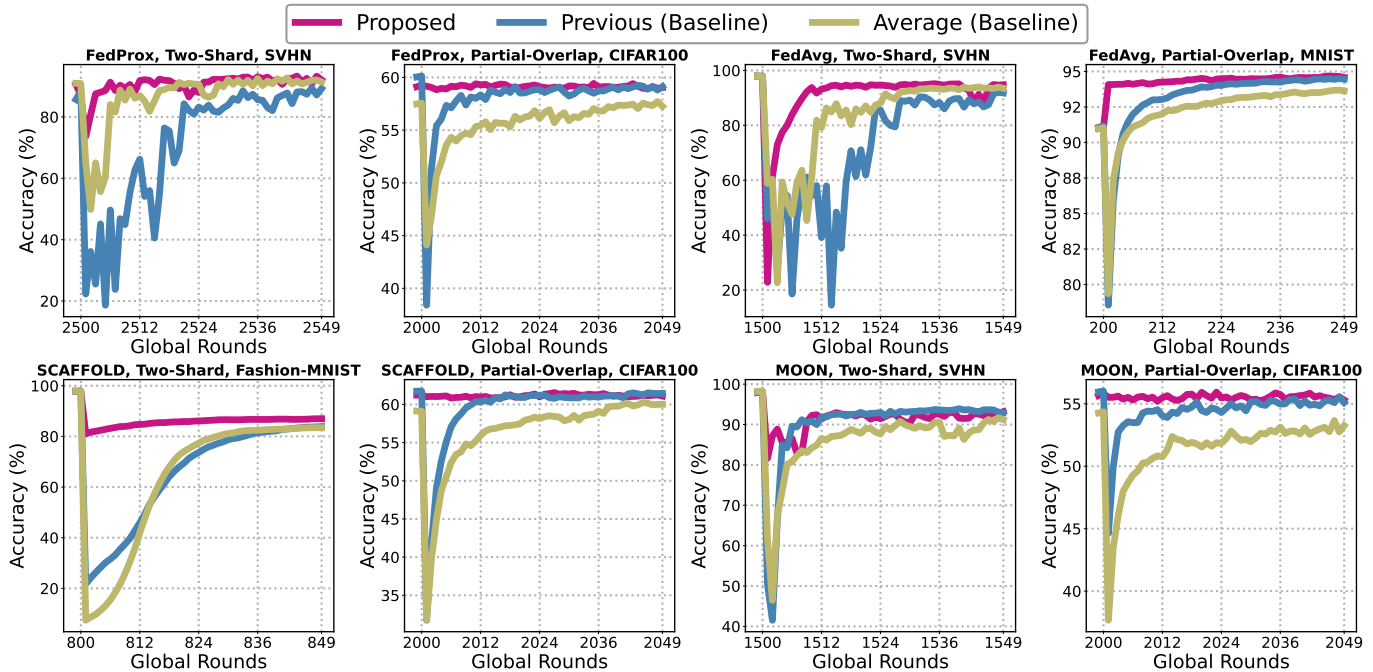


Fig. 5. Performance comparison of the proposed algorithm implemented with four FL algorithms under “Two-Shard” and “Partial-Overlap” label distributions across selected datasets. The results demonstrate the robustness of our proposed scheme to dynamic data distributions caused by client arrivals and departures.

Table XIII presents the results of applying Table 1 with FedAvg for 20 clients on the TinyImageNet dataset [50]. The baseline method used is “Average.” These results highlight the effectiveness of Table 1 in handling scenarios with a larger client population and a more complex dataset using a more advanced model ResNet34.

Table XIV shows the results for 100 clients for Algorithm 1 integrated with FedProx, FedAvg, SCAFFOLD, and MOON on the MNIST and Fashion-MNIST datasets, using 100 clients under the Partial-Overlap label distribution. Performance is evaluated over three transitions for each dataset.

Figure 6 highlights the performance of Algorithm 1 in more selected scenarios and illustrates the advantages of the proposed algorithm for all FL algorithms during periods of pronounced performance drops or gains due to data distribution shifts. The algorithm prioritizes models trained on past distributions that share similarities with the current one, enabling the initial model to adapt more quickly to the new distribution and consistently outperforming baseline approaches. These results underscore the robustness and effectiveness of the proposed approach across diverse FL algorithms, datasets, models, and dynamic data distributions.

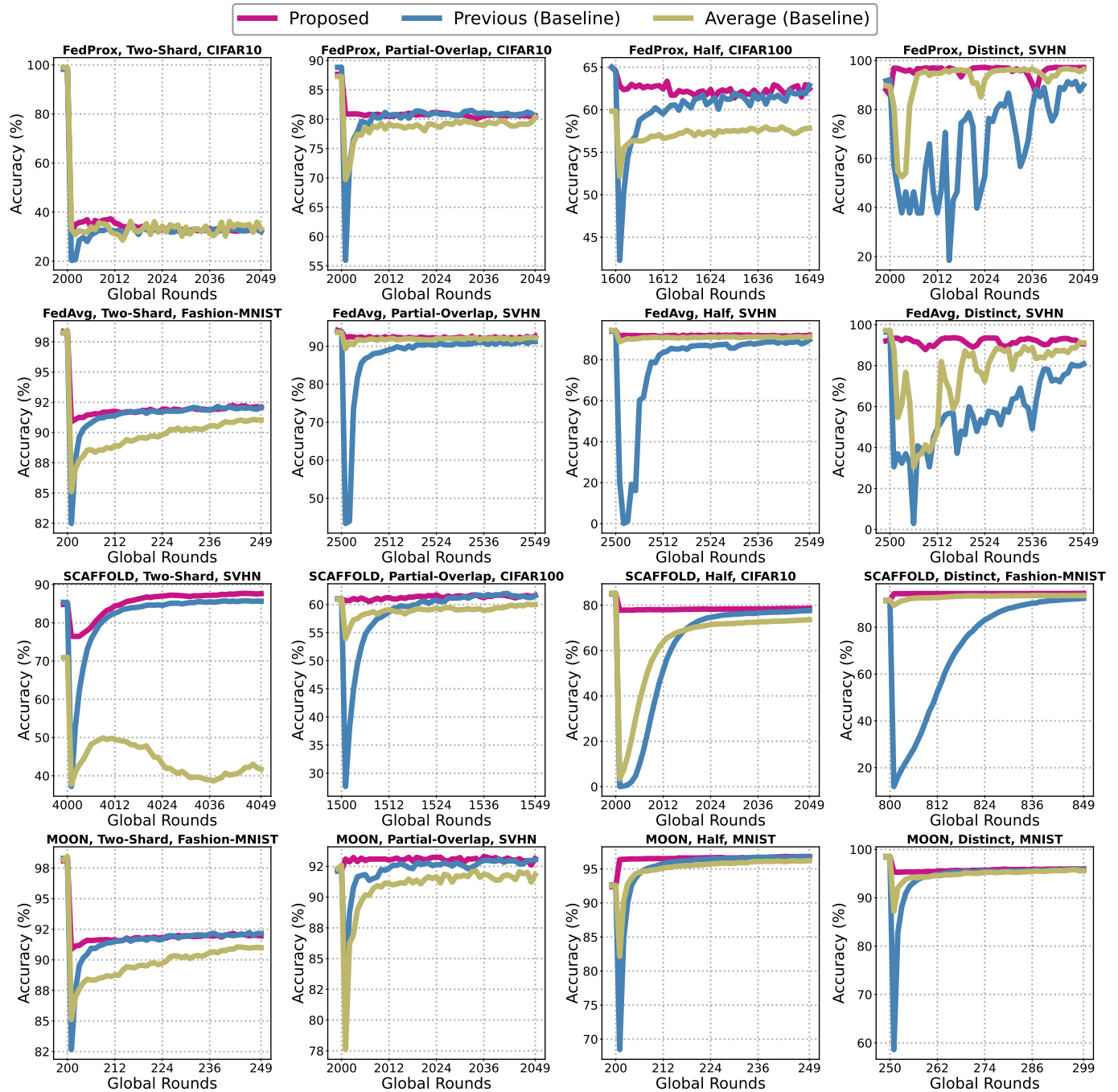


Fig. 6. Performance comparison of the proposed algorithm implemented with four FL algorithms under all label distributions across more selected datasets. The results demonstrate the robustness of our proposed scheme to dynamic data distributions caused by client arrivals and departures.

TABLE X
PERFORMANCE COMPARISON OF IMPLEMENTING ALGORITHM 1 WITH MOON, FEDPROX, SCAFFOLD AND FEDACG UNDER DIFFERENT LABEL DISTRIBUTIONS FOR MNIST, FASHION-MNIST (FMNIST), SVHN, AND CIFAR-10 DATASET FOR 100 CLIENTS.

Dataset	Overlap	Dirichlet α	FL Alg.	Second Session Transition				Fourth Session Transition			
				Proposed	Continuous	Previous	Average	Proposed	Continuous	Previous	Average
MNIST	0.0	0.3	MOON	92.04±0.24	76.92±0.34	57.82±1.23	64.19±0.85	93.08±0.17	81.93±0.42	69.35±0.75	77.92±0.72
			FedProx	92.08±0.24	76.92±0.34	58.92±1.15	66.45±0.94	92.86±0.26	81.93±0.42	70.12±0.76	79.51±0.66
			SCAFFOLD	90.69±0.42	84.30±3.26	50.36±1.91	49.97±2.04	91.95±0.39	86.39±2.63	64.93±1.35	68.55±1.45
			FedACG	93.60±0.21	76.92±0.34	60.92±0.71	71.74±0.51	94.14±0.17	81.93±0.42	70.17±0.50	82.66±0.49
	0.7	MOON	92.07±0.24	77.33±0.41	58.26±1.18	64.78±0.77	93.09±0.17	82.17±0.37	69.65±0.69	78.30±0.59	
		FedProx	92.10±0.24	77.33±0.41	59.20±1.13	66.76±0.89	92.88±0.26	82.17±0.37	70.33±0.73	79.72±0.58	
		SCAFFOLD	91.18±0.46	89.12±0.77	50.85±1.74	51.03±2.03	92.31±0.27	88.76±0.84	65.27±1.18	69.68±1.32	
		FedACG	93.60±0.21	77.33±0.41	61.15±0.65	72.02±0.50	94.16±0.18	82.17±0.37	70.36±0.49	82.83±0.46	
	0.2	0.3	MOON	92.58±0.16	80.98±0.27	70.49±0.97	72.59±0.97	93.56±0.17	84.65±0.21	79.21±0.63	82.68±0.54
			FedProx	92.61±0.15	80.98±0.27	71.42±0.89	74.21±0.93	93.27±0.18	84.65±0.21	79.71±0.65	83.52±0.47
			SCAFFOLD	91.32±0.30	86.65±3.84	64.11±1.24	61.30±2.11	92.50±0.30	87.27±1.50	75.88±0.75	75.74±0.95
			FedACG	93.98±0.14	80.98±0.27	72.61±0.66	77.79±0.65	94.48±0.10	84.65±0.21	79.45±0.42	85.73±0.35
0.7	MOON	92.61±0.16	81.29±0.28	70.80±0.94	73.00±0.95	93.57±0.16	84.82±0.21	79.39±0.63	82.86±0.53		
	FedProx	92.63±0.14	81.29±0.28	71.66±0.88	74.42±0.92	93.28±0.19	84.82±0.21	79.82±0.65	83.66±0.47		
	SCAFFOLD	91.72±0.32	90.06±0.86	64.59±1.28	61.98±1.94	92.78±0.24	89.85±0.82	76.13±0.80	76.28±0.98		
	FedACG	93.99±0.15	81.29±0.28	72.81±0.68	77.97±0.68	94.51±0.13	84.82±0.21	79.57±0.43	85.83±0.36		
FMNIST	0.0	0.3	MOON	83.13±0.09	59.36±0.90	77.09±0.40	77.84±0.49	84.88±0.19	64.58±0.25	79.48±0.29	80.04±0.42
			FedProx	83.19±0.08	59.36±0.90	77.74±0.37	78.57±0.50	84.22±0.21	64.58±0.25	79.90±0.32	80.52±0.46
			SCAFFOLD	77.80±0.42	65.94±5.97	47.74±0.88	47.93±1.88	79.88±0.17	74.69±4.63	53.64±0.54	60.72±0.93
			FedACG	85.10±0.22	59.36±0.90	77.61±0.25	80.44±0.38	85.82±0.07	64.58±0.25	80.01±0.31	82.22±0.35
	0.7	MOON	83.29±0.11	60.72±0.80	77.59±0.31	78.32±0.40	84.89±0.18	65.36±0.38	79.86±0.28	80.26±0.41	
		FedProx	83.33±0.13	60.72±0.80	78.16±0.35	78.93±0.43	84.29±0.15	65.36±0.38	80.28±0.34	80.72±0.38	
		SCAFFOLD	78.43±0.54	68.57±4.87	47.32±1.12	48.45±1.62	80.49±0.40	70.81±7.27	53.02±0.86	61.01±1.13	
		FedACG	85.17±0.25	60.72±0.80	78.03±0.29	80.68±0.39	85.81±0.13	65.36±0.38	80.45±0.26	82.41±0.29	
	0.2	0.3	MOON	82.88±0.15	72.53±0.29	74.83±0.31	76.78±0.59	84.30±0.14	75.78±0.16	77.15±0.17	79.48±0.53
			FedProx	82.91±0.13	72.53±0.29	75.55±0.28	77.69±0.63	83.81±0.19	75.78±0.16	77.63±0.16	79.96±0.54
			SCAFFOLD	77.35±0.53	69.90±6.23	55.82±1.59	50.39±4.48	79.45±0.21	70.79±4.93	61.12±1.40	61.10±2.25
			FedACG	84.63±0.12	72.53±0.29	76.09±0.23	79.21±0.37	85.36±0.16	75.78±0.16	77.92±0.21	81.54±0.22
0.7	MOON	83.02±0.15	73.73±0.26	75.38±0.20	77.31±0.61	84.36±0.16	76.53±0.15	77.54±0.21	79.79±0.51		
	FedProx	83.04±0.15	73.73±0.26	75.99±0.19	78.14±0.73	83.95±0.22	76.53±0.15	78.06±0.21	80.22±0.56		
	SCAFFOLD	77.88±0.54	74.14±7.98	55.77±1.46	50.02±4.42	79.85±0.21	74.03±6.67	60.69±1.26	60.68±1.80		
	FedACG	84.70±0.14	73.73±0.26	76.45±0.22	79.65±0.37	85.41±0.13	76.53±0.15	78.31±0.16	81.82±0.25		
SVHN	0.0	0.3	MOON	92.98±0.08	86.82±0.75	82.65±4.35	82.32±3.62	93.69±0.13	89.13±0.27	83.80±0.06	87.56±2.06
			FedProx	91.78±0.16	86.54±0.18	86.87±2.00	88.26±0.36	92.36±0.12	87.93±0.28	89.25±1.10	90.59±0.38
			SCAFFOLD	89.70±2.57	50.14±13.22	80.23±8.59	84.29±1.56	91.54±1.28	84.76±2.61	87.11±3.05	88.71±0.63
			FedACG	93.09±0.16	86.56±0.23	80.67±2.41	86.95±2.77	93.48±0.27	87.95±0.28	75.82±1.48	90.30±1.67
	0.7	MOON	93.21±0.18	88.72±0.33	84.88±3.19	87.03±3.18	93.95±0.13	90.37±0.21	87.69±1.98	90.44±1.50	
		FedProx	92.08±0.13	87.54±0.23	87.12±1.39	88.90±0.30	92.68±0.09	88.75±0.21	89.83±0.94	90.91±0.19	
		SCAFFOLD	92.06±0.61	68.61±11.01	86.32±3.01	85.88±1.23	93.13±0.45	90.40±1.04	90.28±1.10	89.47±0.86	
		FedACG	93.41±0.19	87.57±0.23	80.39±3.72	88.17±2.16	93.80±0.18	88.73±0.23	76.94±5.63	91.25±1.04	
	0.2	0.3	MOON	93.23±0.18	88.20±0.90	84.16±2.15	81.18±2.49	93.86±0.19	90.22±0.39	86.34±3.65	84.40±1.80
			FedProx	92.10±0.21	87.44±0.81	88.04±2.09	85.45±1.25	92.75±0.21	89.05±0.50	90.01±1.32	88.57±0.57
			SCAFFOLD	90.28±1.63	61.27±19.08	83.62±2.11	86.01±1.59	91.90±1.32	85.59±4.43	89.27±1.20	89.81±1.06
			FedACG	93.34±0.25	87.43±0.84	84.39±1.47	89.51±1.49	93.66±0.20	89.06±0.48	89.77±1.96	91.29±0.80
0.7	MOON	93.54±0.24	89.92±0.32	85.92±2.37	85.59±2.71	94.24±0.19	91.20±0.22	89.17±1.73	88.30±1.71		
	FedProx	92.39±0.21	88.36±0.36	88.52±2.37	86.70±1.25	93.02±0.19	89.85±0.27	90.68±1.49	89.35±0.71		
	SCAFFOLD	92.10±0.82	75.97±8.03	87.49±1.29	86.91±0.86	93.30±0.56	89.57±1.58	90.79±0.46	90.60±0.20		
	FedACG	93.64±0.24	88.38±0.36	84.67±2.49	90.33±1.14	93.97±0.23	89.88±0.27	87.79±1.84	91.85±0.63		
CIFAR-10	0.0	0.3	MOON	61.29±1.22	57.89±0.82	48.09±0.39	59.17±1.51	64.73±0.71	63.34±0.53	53.91±0.92	61.77±1.53
			FedProx	61.40±1.09	57.96±0.68	45.94±0.76	59.18±1.37	64.06±0.75	63.38±0.57	51.16±0.56	61.91±1.31
			SCAFFOLD	68.44±0.73	68.93±1.91	53.67±0.64	65.15±1.10	70.49±0.59	72.52±1.55	55.75±0.87	67.62±0.95
			FedACG	61.88±2.33	57.88±0.75	44.12±1.29	64.33±1.53	64.05±2.01	63.33±0.40	45.60±1.78	65.57±1.50
	0.7	MOON	66.28±0.51	61.39±0.73	49.03±1.55	63.70±0.46	69.46±0.45	67.11±0.51	57.95±1.08	66.00±0.53	
		FedProx	66.30±0.64	61.54±0.71	46.50±1.17	64.01±0.67	69.13±0.78	67.09±0.44	54.31±1.17	66.56±0.54	
		SCAFFOLD	72.95±0.68	71.91±0.81	57.37±0.84	69.29±0.86	75.12±0.81	76.43±0.38	59.80±0.57	71.71±0.89	
		FedACG	70.35±0.80	61.46±0.74	47.91±1.35	68.17±0.50	73.23±0.60	67.09±0.41	49.10±1.29	69.73±0.33	
	0.2	0.3	MOON	54.39±1.21	51.64±0.93	51.54±1.02	53.65±0.92	59.17±1.25	57.26±0.93	56.34±0.66	56.85±0.84
			FedProx	55.26±1.80	51.74±0.88	50.40±0.99	53.29±0.80	59.97±1.44	57.42±0.74	54.30±0.96	56.91±0.68
			SCAFFOLD	67.35±0.65	63.67±3.23	52.91±1.16	62.49±0.88	69.36±0.73	68.02±2.04	54.60±1.12	65.57±0.90
			FedACG	59.33±2.61	51.48±0.88	48.80±1.07	55.33±0.99	62.01±2.09	57.31±0.67	49.07±2.10	59.35±0.73
0.7	MOON	61.78±1.59	57.64±0.52	53.14±1.17	58.49±0.82	66.10±1.53	64.19±0.45	59.72±0.74	60.73±0.73		
	FedProx	63.81±1.31	57.73±0.50	52.35±0.95	58.70±0.71	66.36±1.13	64.24±0.44	58.05±0.72	61.36±0.66		
	SCAFFOLD	71.33±0.81	69.56±0.60	58.65±0.59	67.46±0.45	73.51±0.74	74.41±1.15	61.05±0.85	70.39±0.38		
	FedACG	66.27±1.49	57.67±0.56	51.04±0.52	61.61±0.39	69.04±1.37	64.20±0.48	53.47±0.73	64.66±0.37		
CIFAR-100	0.0	0.3	MOON	38.74±0.52	32.35±0.52	37.40±0.61	36.09±0.58	42.21±0.55	38.76±0.46	43.42±0.85	39.70±0.49
			FedProx	38.38±0.46	32.21±0.46	35.87±1.13	35.41±0.56	41.94±0.40	38.83±0.68	42.04±1.14	39.23±0.54
			SCAFFOLD	45.03±0.34	46.10±0.80	44.21±0.65	42.32±0.56	48.32±0.76	50.89±0.50	49.94±0.34	45.49±0.50
			FedACG	47.07±0.37	32.30±0.19	26.86±0.57	41.86±0.80	50.10±0.46	38.90±0.36	38.18±0.86	45.26±0.55
	0.7	MOON	41.25±0.65	35.54±0.52	39.22±1.20	38.10±0.64	44.99±0.89	41.91±0.49	44.65±1.87	41.43±0.54	
		FedProx	41.11±0.36	35.62±0.53	37.07±1.67	37.70±0.65	44.59±0.54	42.02±0.49	42.71±1.32	41.60±0.72	
		SCAFFOLD	47.60±0.43	47.85±0.46	46.91±0.58	44.16±0.59	50.71±0.70	51.37±0.44	52.50±0.81	47.79±0.42	
		FedACG	49.57±0.40	35.58±0.48	28.44±0.62	44.35±0.94	52.30±0.78	42.13±0.41	39.32±1.57	47.63±0.51	
	0.2	0.3	MOON	44.46±0.65	39.95±0.81	44.49±0.64	35.92±1.05	47.35±0.75	45.93±0.27	49.99±0.81	39.61±0.47
			FedProx	44.18±1.00	40.27±0.38	45.57±0.99	38.69±0.36	47.40±0.90	45.92±0.28	50.22±0.34	42.32±0.47
			SCAFFOLD	49.40±0.53	49.20±0.90	47.35±1.00	43.93±0.43	52.22±0.38	51.88±0.55	52.19±1.35	47.31±0.41
			FedACG	51.73±0.22	39.95±0.83	39.87±1.36	43.93±1.12	53.64±0.19	45.62±0.70	46.71±0.92	48.03±1.22
0.7	MOON	47.27±0.41	43.14±0.31	44.98±0.29	37.88±0.66						

TABLE XI
PERFORMANCE COMPARISON OF IMPLEMENTING ALGORITHM 1 WITH FEDPROX, FEDAVG, SCAFFOLD AND MOON UNDER DIFFERENT LABEL DISTRIBUTIONS AND DATASETS. PERFORMANCE IS MEASURED ACROSS 3 TRANSITIONS FOR EACH DATASET.

FL Algorithm	Label Distribution	Dataset (Model)	1st Transition			2nd Transition			3rd Transition		
			Proposed	Previous	Average	Proposed	Previous	Average	Proposed	Previous	Average
FedProx	Two-Shard	MNIST (MLP)	98.45	96.4	98.24	94.77	90.72	93.19	98.56	96.53	98.4
		Fashion-MNIST (MLP)	92.04	90.31	88.89	97.59	96.38	97.33	95.39	93.54	94.58
		SVHN (CNN)	86.52	40.13	72.7	97.44	84.53	95.08	95.8	55.16	83.08
		CIFAR10 (ResNet18)	41.64	35.32	39.68	46.26	35.62	44.62	82.58	58.34	78.3
		CIFAR100 (ResNet18)	58.46	56.68	51.07	49.28	46.52	47.7	52.73	48.35	51.49
	Partial-Overlap	MNIST (MLP)	62.88	56.16	56.23	64.27	57.14	53.96	63.53	57.41	56.81
		Fashion-MNIST (MLP)	87.06	83.79	86.78	88.06	85.52	84.78	87.2	84.33	86.89
		SVHN (CNN)	92.4	76.09	91.72	93.64	68.67	92.35	92.51	71.79	92.02
		CIFAR10 (ResNet18)	81.5	77.05	77.31	86.99	83.88	84.97	81.69	79.84	77.62
		CIFAR100 (ResNet18)	59.09	54.94	52.23	59.22	55.09	56.13	59.34	56.11	53.34
FedAvg	Two-Shard	MNIST (MLP)	98.45	96.4	98.24	94.77	90.72	93.19	98.56	96.53	98.4
		Fashion-MNIST (MLP)	92.04	90.31	88.89	97.59	96.38	97.33	95.39	93.54	94.58
		SVHN (CNN)	76.53	51.03	56.65	83.45	39.58	72.65	95.87	42.97	85.15
		CIFAR10 (ResNet18)	41.98	32.77	41.05	51.01	36.57	48.57	82.51	64.03	81.04
		CIFAR100 (ResNet18)	47.88	44.29	46.87	49.63	46.04	47.64	52.18	48.43	51.17
	Partial-Overlap	MNIST (MLP)	93.81	89.65	89.33	91.11	87.46	90.35	94.16	90.1	90.67
		Fashion-MNIST (MLP)	87.58	85.06	83.04	86.77	83.88	86.49	87.64	85.59	84.16
		SVHN (CNN)	92.27	79.11	89.94	93.67	82.01	91.46	92.48	77.2	91.47
		CIFAR10 (ResNet18)	85.87	82.35	83.84	79.94	77.1	75.31	85.87	82.9	84.41
		CIFAR100 (ResNet18)	56.94	53.29	54.31	57.25	54.17	51.71	57.35	54.41	54.6
SCAFFOLD	Two-Shard	MNIST (MLP)	97.97	51.69	96.73	92.27	42.16	44.86	98.32	54.78	97.26
		Fashion-MNIST (MLP)	84.24	36.59	22.94	96.89	51.82	96.18	92.29	52.41	45.45
		SVHN (CNN)	79.23	69.2	47.94	95.32	90.76	73.11	93.96	88.37	73.25
		CIFAR10 (ResNet18)	46.63	10.74	23.31	92.39	38.32	90.59	56.11	12.66	24.98
		CIFAR100 (ResNet18)	21.63	5.61	9.59	35.75	21.3	19.42	26.18	7.69	11.98
	Partial-Overlap	MNIST (MLP)	85.72	61.6	71.39	89.66	77.03	53.64	87.1	69.45	72.93
		Fashion-MNIST (MLP)	86.67	62.41	74.68	87.54	63.48	68.97	87.64	65.2	74.91
		SVHN (CNN)	90.33	84.02	73.88	91.9	89.05	80.91	91.33	85.83	74.68
		CIFAR10 (ResNet18)	72.64	37.95	42.06	79.12	39.31	69.88	74.52	40.29	49.57
		CIFAR100 (ResNet18)	61.03	52.56	48.94	61.16	53.54	58.66	60.79	53.99	53.2
MOON	Two-Shard	MNIST (MLP)	98.15	96.54	98.04	98.38	96.55	98.24	98.52	96.48	98.39
		Fashion-MNIST (MLP)	92.08	90.28	88.84	97.42	96.47	97.31	95.36	93.54	94.53
		SVHN (CNN)	87.0	78.61	75.72	69.51	64.57	54.88	93.49	90.2	89.87
		CIFAR10 (ResNet18)	44.03	40.53	39.42	51.31	43.46	41.82	85.0	71.45	73.54
		CIFAR100 (ResNet18)	57.94	56.05	44.18	45.8	43.81	44.71	62.06	60.56	53.54
	Partial-Overlap	MNIST (MLP)	93.85	89.65	89.33	91.1	87.64	90.35	94.12	90.2	90.67
		Fashion-MNIST (MLP)	87.6	85.06	83.04	86.66	83.66	86.49	88.01	85.53	84.16
		SVHN (CNN)	92.96	90.41	88.39	91.74	87.97	90.77	93.18	91.25	90.25
		CIFAR10 (ResNet18)	85.53	83.59	84.67	79.28	77.57	76.04	79.37	78.44	76.11
		CIFAR100 (ResNet18)	55.52	52.58	47.77	55.27	52.22	52.7	55.72	53.49	49.01

TABLE XII
PERFORMANCE COMPARISON OF FEDPROX, FEDAVG, SCAFFOLD, AND MOON UNDER “HALF” AND “DISTINCT” LABEL DISTRIBUTIONS ACROSS VARIOUS DATASETS. PERFORMANCE IS EVALUATED OVER THREE TRANSITIONS FOR EACH DATASET.

FL Algorithm	Label Distribution	Dataset (Model)	1st Transition			2nd Transition			3rd Transition		
			Proposed	Previous	Average	Proposed	Previous	Average	Proposed	Previous	Average
FedProx	Half	MNIST (MLP)	96.02	90.12	92.45	96.29	90.56	93.59	93.25	88.17	92.45
		Fashion-MNIST (MLP)	90.97	86.02	90.17	86.62	85.06	84.2	91.29	86.67	90.26
		SVHN (CNN)	93.23	27.0	92.18	91.64	17.15	90.98	93.53	69.5	92.75
		CIFAR10 (ResNet18)	86.32	48.83	83.59	90.38	54.74	87.64	87.68	58.41	84.62
	CIFAR100 (ResNet18)	62.88	56.16	56.23	64.27	57.14	53.96	63.53	57.41	56.81	
	Distinct	MNIST (MLP)	98.05	92.75	97.71	95.98	88.77	93.96	94.11	85.66	90.54
Fashion-MNIST (MLP)		95.5	92.4	95.0	95.8	90.59	94.56	94.02	87.36	90.73	
SVHN (CNN)		92.25	45.18	67.51	87.91	38.45	63.85	92.24	42.7	60.68	
FedAvg	Half	MNIST (MLP)	96.03	90.12	92.45	92.56	87.83	92.45	96.21	90.56	93.59
		Fashion-MNIST (MLP)	86.24	84.54	82.54	90.29	86.12	89.91	90.5	86.62	90.1
		SVHN (CNN)	91.63	71.49	88.78	93.54	51.98	91.07	91.98	42.34	90.55
		CIFAR10 (ResNet18)	90.19	70.15	88.08	86.23	77.41	81.67	90.03	73.55	89.25
	CIFAR100 (ResNet18)	57.41	52.95	54.37	57.09	53.7	51.07	57.48	53.38	54.44	
	Distinct	MNIST (MLP)	97.97	93.03	97.57	95.72	89.19	93.65	94.04	86.11	90.4
Fashion-MNIST (MLP)		95.81	90.66	94.44	93.88	87.5	90.56	95.8	92.0	94.86	
SVHN (CNN)		94.99	49.88	80.62	91.9	38.94	58.53	87.21	32.71	66.47	
SCAFFOLD	Half	MNIST (MLP)	85.53	29.8	82.93	92.58	57.81	30.18	89.08	51.43	84.39
		Fashion-MNIST (MLP)	77.18	36.71	28.55	83.35	65.31	77.91	79.51	40.82	42.19
		SVHN (CNN)	91.66	86.87	76.06	89.86	84.79	80.25	93.04	87.31	87.18
		CIFAR10 (ResNet18)	78.63	17.35	34.76	84.62	19.59	79.32	80.13	20.86	49.7
	CIFAR100 (ResNet18)	28.92	9.97	18.74	31.11	13.3	6.44	34.23	13.84	21.62	
	Distinct	MNIST (MLP)	96.95	50.5	95.35	93.08	22.24	60.96	91.36	21.06	22.78
Fashion-MNIST (MLP)		94.08	32.05	91.66	93.28	13.81	53.5	91.72	29.1	33.07	
MOON	Half	MNIST (MLP)	96.06	90.16	92.45	92.64	87.78	92.45	96.29	90.46	93.59
		Fashion-MNIST (MLP)	86.12	84.43	82.54	90.33	85.79	89.91	86.31	84.96	83.75
		SVHN (CNN)	93.64	89.35	89.95	92.11	87.3	91.18	93.63	90.54	91.37
		CIFAR10 (ResNet18)	89.0	85.77	88.26	84.89	81.08	81.53	89.16	86.67	88.51
	CIFAR100 (ResNet18)	54.9	52.27	53.8	55.95	52.75	48.99	55.05	52.63	54.07	
	Distinct	MNIST (MLP)	95.67	88.67	93.56	94.07	85.7	90.2	95.63	90.65	94.32
Fashion-MNIST (MLP)		95.76	90.14	94.4	93.86	86.83	90.06	95.66	91.76	94.85	

TABLE XIII
PERFORMANCE OF ALGORITHM 1 WITH FEDAVG UNDER “HALF” AND “PARTIAL-OVERLAP” LABEL DISTRIBUTIONS FOR THE TINYIMAGENET DATASET WITH 20 CLIENTS. PERFORMANCE IS MEASURED ACROSS THREE TRANSITIONS FOR EACH DATASET.

Label Distribution	Dataset (Model)	1st Transition		2nd Transition		3rd Transition	
		Proposed	Previous	Proposed	Previous	Proposed	Previous
Half	TinyImageNet (ResNet34)	80.72	72.81	77.77	72.24	80.43	73.42
Partial-Overlap	TinyImageNet (ResNet34)	92.27	79.11	93.67	82.01	92.48	77.2

TABLE XIV
PERFORMANCE COMPARISON OF ALGORITHM 1 INTEGRATED WITH FEDPROX, FEDAVG, SCAFFOLD, AND MOON ON THE MNIST AND FASHION-MNIST DATASETS, UTILIZING 100 CLIENTS FOR FEDPROX, FEDAVG, AND MOON, AND 50 CLIENTS FOR SCAFFOLD UNDER THE PARTIAL-OVERLAP LABEL DISTRIBUTION. PERFORMANCE IS EVALUATED ACROSS THREE TRANSITIONS FOR EACH DATASET.

FL Algorithm	Dataset (Model)	1st Transition			2nd Transition			3rd Transition		
		Proposed	Previous	Average	Proposed	Previous	Average	Proposed	Previous	Average
FedProx	MNIST (MLP)	94.09	89.53	89.35	91.36	87.4	90.45	94.33	89.92	90.78
	Fashion-MNIST (MLP)	87.88	85.13	83.37	87.14	83.86	86.76	88.08	85.57	84.65
FedAvg	MNIST (MLP)	90.86	86.15	90.25	94.09	89.53	89.35	91.36	87.4	90.45
	Fashion-MNIST (MLP)	86.55	82.78	86.4	87.88	85.13	83.37	87.14	83.86	86.76
SCAFFOLD	MNIST (MLP)	64.82	33.15	52.67	82.67	62.47	30.18	74.04	50.77	59.66
MOON	MNIST (MLP)	91.36	87.4	90.45	94.33	89.92	90.78	91.55	87.87	90.55
	Fashion-MNIST (MLP)	87.14	83.86	86.75	88.07	85.57	84.65	87.31	84.34	86.9